Check for updates

AGU ADVANCING EARTH AND SPACE SCIENCE

Tectonics

RESEARCH ARTICLE
10.1029/2019TC005958

Key Points:
- Andean retroarc basin was structurally partitioned into isolated hinterland and broken foreland basins during subduction shallowing
- Clastic progradational deposystems and orogenic unroofing signatures are associated with sequential Andean deformation
- Flat slab subduction drove the advance of the Andean magmatic front >450 km eastward into the foreland at 10 Ma

Supporting Information:
- Supporting Information S1
- Table S1
- Table S2
- Table S3
- Table S4
- Table S5
- Table S6

Correspondence to:
T. N. Capaldi,
tomas.capaldi@unlv.edu

Citation:
Capaldi, T. N., Horton, B. K., McKenzie, N. R., Mackaman-Lofland, C., Stockli, D. F., Ortiz, G., & Alvarado, P. (2020). Neogene retroarc foreland basin evolution, sediment provenance, and magmatism in response to flat slab subduction, western Argentina. *Tectonics*, *39*, e2019TC005958. https://doi.org/10.1029/2019TC005958

Received 1 NOV 2019
Accepted 13 MAY 2020
Accepted article online 31 MAY 2020

©2020. American Geophysical Union. All Rights Reserved.

Neogene Retroarc Foreland Basin Evolution, Sediment Provenance, and Magmatism in Response to Flat Slab Subduction, Western Argentina

Tomas N. Capaldi[1,2], Brian K. Horton[1,3], N. Ryan McKenzie[4], Chelsea Mackaman-Lofland[1], Daniel F. Stockli[1], Gustavo Ortiz[5], and Patricia Alvarado[5]

[1]Department of Geological Sciences, Jackson School of Geosciences, University of Texas at Austin, Austin, TX, USA, [2]Now at Department of Geoscience, University of Nevada, Las Vegas, Las Vegas, NV, USA, [3]Institute for Geophysics, Jackson School of Geosciences, University of Texas at Austin, Austin, TX, USA, [4]Department of Earth Sciences, University of Hong Kong, Hong Kong, China, [5]CONICET and Universidad Nacional de San Juan (CIGEOBIO), Departamento de Geofísica y Astronomía, FCEFN-UNSJ, San Juan, Argentina

Abstract Understanding the effects of flat slab subduction on mountain building, arc magmatism, and basin evolution is fundamental to convergent-margin tectonics, with implications for potential feedbacks among geodynamic, magmatic, and surface processes. New stratigraphic and geochronological constraints on Cenozoic sedimentation and magmatism in the southern Central Andes of Argentina (31°S) reveal shifts in volcanism, foreland/hinterland basin development, sediment accumulation, and provenance as the retroarc region was structurally partitioned during slab flattening. Detrital zircon U-Pb age distributions from the western (Calingasta basin), central (Talacasto and Albarracín basins), and eastern (Bermejo foreland basin) segments of the retroarc basin system preserve syndepositional volcanism and orogenic unroofing of multiple tectonic provinces. Initial shortening-related exhumation of the Principal Cordillera at 24–17 Ma was recorded by the accumulation of distal eolian deposits bearing Oligocene–Eocene zircons from the Andean magmatic arc. The Calingasta basin chronicled volcanism and basement shortening in the Frontal Cordillera at ~17–11 Ma, as marked by an upward coarsening succession of fluvial to alluvial fan deposits with a sustained zircon U-Pb age component that matches pervasive Permian-Triassic bedrock in the hinterland. An ~450 km eastward inboard sweep of volcanism at 11 Ma coincided with the inception of flat slab subduction, and subsequent thin-skinned shortening in the Precordillera fold-thrust belt that exhumed wedge-top deposits and induced cratonward (eastward) advance of flexural subsidence into the Bermejo foreland basin. This foreland basin was structurally partitioned as basement uplifts of the Sierras Pampeanas transformed a fluvial megafan sediment routing network into smaller isolated alluvial fan systems fed by adjacent basement blocks.

1. Introduction

Geodynamic models and past geologic examples indicate that many convergent plate boundaries experience phases of subhorizontal or flat subduction (Cross & Pilger, 1982; Dickinson & Snyder, 1978; Gurnis, 1992; Gutscher et al., 2000; Horton, 2018a; Martinod et al., 2010; Ramos et al., 2002; Ramos & Folguera, 2009; Schellart, 2017). Potential drivers of flat slab subduction include accelerated relative plate convergence, rapid trenchward advance of the overriding plate, mantle wedge dynamic pressure (slab suction), and subduction of buoyant oceanic lithosphere of large thickness, low density, or young age (Bishop et al., 2017; Guillaume et al., 2009; Iaffaldano et al., 2006; Jarrard, 1986; Schellart et al., 2007; van Hunen et al., 2002). Many studies have observed genetic links between shallowing subduction and the inboard advance and shutoff of arc magmatism (e.g., Coney, 1978; Coney & Reynolds, 1977; Constenius, 1996; Constenius et al., 2003; Dickinson & Snyder, 1978; Finzel et al., 2011; Humphreys, 1995; Kapp & Decelles, 2019; Saleeby, 2003). The time-space record of arc magmatism tracks the locus of dehydration melting above the leading inboard hinge of the subducted slab (marking the boundary between the shallow flat slab and deeper steep-slab segments). Basal traction and end-load stresses exerted by flat slab subduction along Cordilleran margins are manifest as zones of intensified crustal shortening, commonly involving basement block uplifts that form major topographic barriers and sediment sources within the structurally partitioned

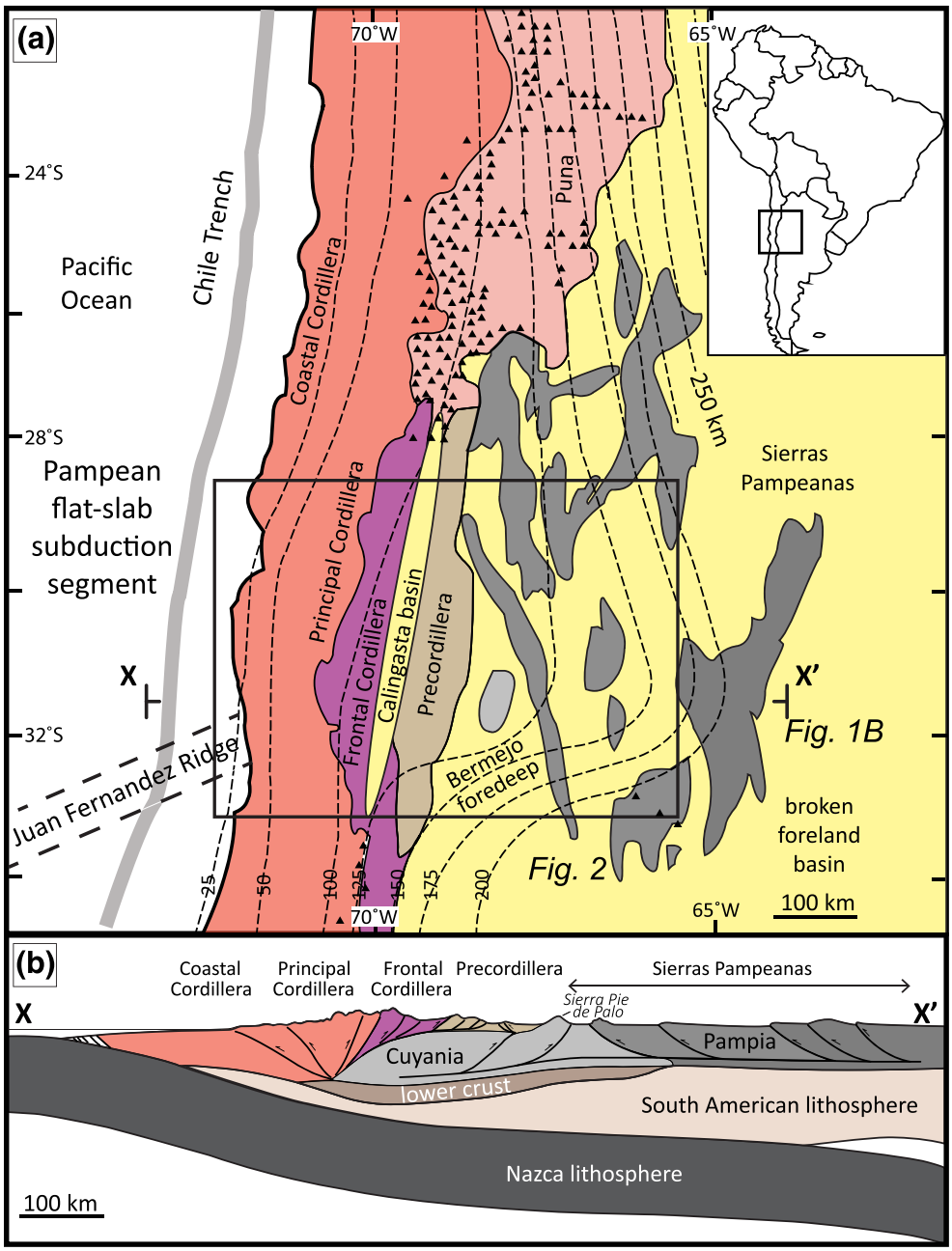

Figure 1. Tectonic setting of the southern Central Andes. (a) Geologic map of major tectonic provinces in the Pampean flat-slab segment of western Argentina and northern Chile, Quaternary Andean arc volcanic centers (black triangles), contoured Benioff zone depths (in kilometers) to the subducted Nazca plate (dashed contour lines), and cross-section X-X′ location (after Ramos et al., 2002). (b) East-west crustal cross section showing various Andean ranges and proposed basement terranes of the south American plate (after Bellahsen et al., 2016).

foreland basin (Axen et al., 2018; Bird, 1984; Carrapa et al., 2008; Dickinson et al., 1988; Erslev, 1993, 2005; Fan & Carrapa, 2014; Jordan, 1995; Lawton, 2008; Yin & Ingersoll, 1997).

The Pampean flat slab segment of the Nazca-South American plate boundary is characterized by shallow-angle subduction, a 27–33°S spatial gap in active volcanism, and distal intraforeland basement uplifts of the Sierras Pampeanas potentially driven by subduction of the Juan Fernandez ridge (Figure 1; Alvarado et al., 2009; Barazangi & Isacks, 1976; Cahill & Isacks, 1992; Jordan et al., 1983; Ramos et al., 2002;

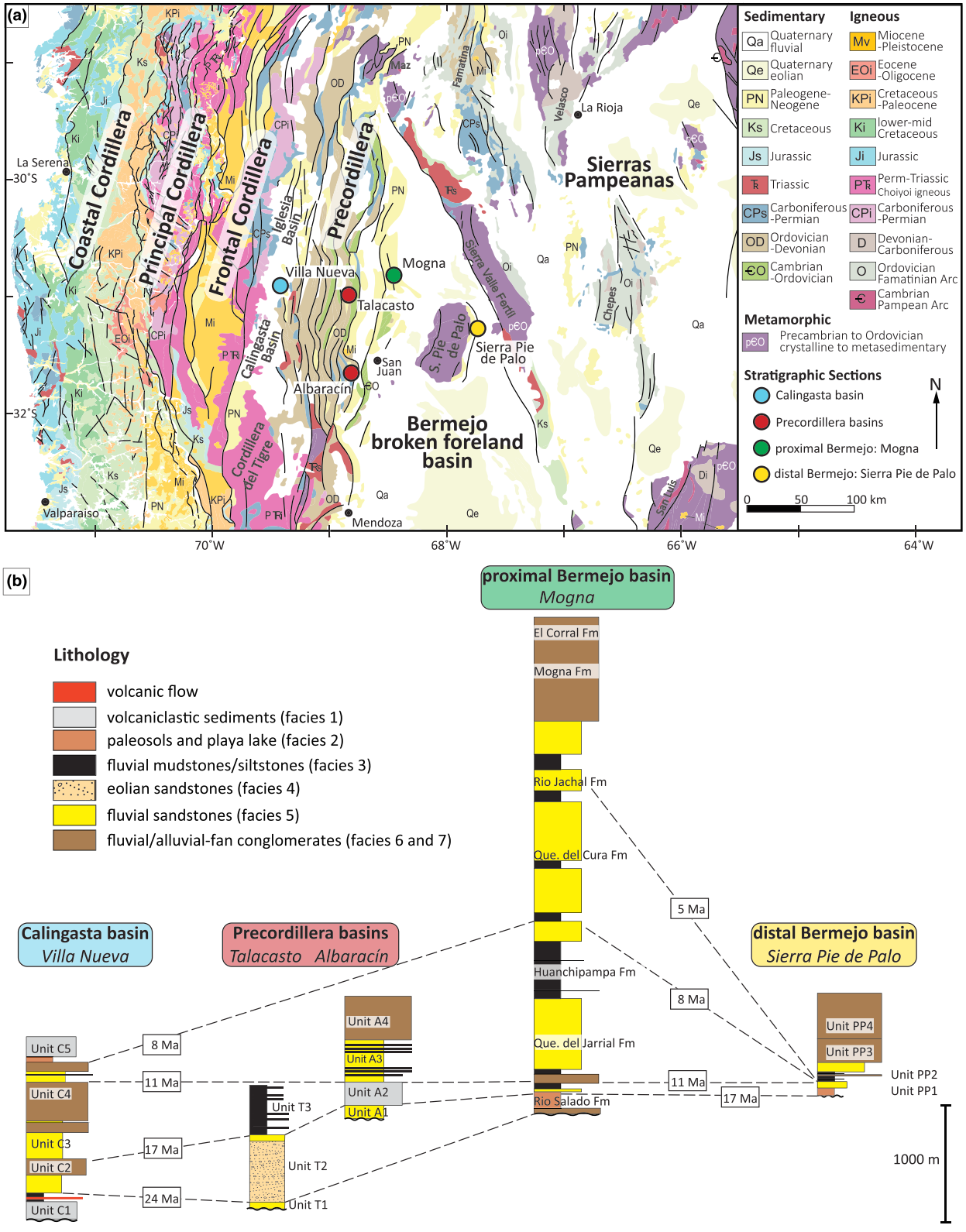

Figure 2. (a) Geologic map of Argentina and Chile (28.5°S to 33°S) displaying major tectonic provinces: Coastal Cordillera, Principal Cordillera, Frontal Cordillera, Calingasta-Iglesia hinterland basin, Precordillera fold-thrust belt, Bermejo foreland basin, and Sierras Pampeanas uplifts, with locations of stratigraphic sections (colored circles) (SEGEMAR, 1999, 2012; Sernageomin, 2003). (b) Schematic stratigraphic sections, facies, and correlated timelines across the Argentina retroarc basin system: Calingasta basin, Precordillera basins, and Bermejo basin.

Ramos & Folguera, 2009). Unresolved issues include the impact of shallow subduction on Andean magmatism, deformation, and basin evolution. Specifically, what was the upper crustal response to flat slab subduction and how do hinterland records compare to foreland records? Although accelerated shortening in the Precordillera fold-thrust belt has been linked to slab shallowing (Allmendinger & Judge, 2014; Fosdick et al., 2015; Hilley et al., 2004; Jordan et al., 1992; Levina et al., 2014), there remains uncertainty in the temporal relationships between the evolving slab geometry and uplift of the Sierras Pampeanas (Carrapa et al., 2008; Ortiz et al., 2015; Ramos et al., 2002; Stevens-Goddard et al., 2018). Whether the separate Precordillera and Sierras Pampeanas structural domains formed in response to synchronous or discrete phases of compression is central to understanding the effects of flat slab subduction and mechanical coupling between the subducting and overriding plate. Further, does the Andean magmatic history support models proposing an inboard sweep and progressive cessation of arc magmatism? This problem is fundamental to geodynamic reconstructions of the Pampean flat slab and potential genetic relationships between magmatism and deformation, including possible orogenic cyclicity and reactivation of inherited structures (Ramos & Folguera, 2009; Ramos et al., 2014; Yáñez et al., 2001). Finally, there is no consensus on whether the foreland basin registered increased subsidence, diminished subsidence, or even dynamic uplift during flat slab subduction (Dávila et al., 2010; Dávila & Lithgow-Bertelloni, 2013, 2015; Finzel et al., 2011; Flament et al., 2015; Heller & Liu, 2016).

This study presents new stratigraphic, sedimentologic, and geochronologic constraints on Cenozoic magmatism, foreland basin sedimentation, and upper crustal exhumation in the southern central Andes (31°S) to evaluate changes in volcanism, sediment provenance, basin subsidence, and deformation. We focus on a series of retroarc basins in western Argentina situated above the Pampean flat slab segment of the southern Central Andes (Figure 1). A 175 km transect at 31°S involves four key basin elements, from west to east: (1) the Calingasta basin between the Frontal Cordillera and Precordillera; (2) foreland basin remnants within the Precordillera thrust belt; (3) the Bermejo foredeep between the Precordillera and Sierras Pampeanas; and (4) the eastern broken foreland basin partitioned by basement uplifts of the Sierras Pampeanas (Figure 2). Constraining changes in sediment provenance and depositional processes within this retroarc basin system affords the opportunity to identify the timing of foreland structural partitioning during slab flattening. This basin record is integrated with new detrital zircon U-Pb data to provide a chronostratigraphic framework in which to track shifts in arc magmatism, shortening, and erosion during the Neogene phase of flat slab subduction.

2. Geologic Framework

At 31°S, the Andes of west-central Argentina (Figure 1) are divided into four N trending provinces, from west to east: (1) a magmatic arc (Principal Cordillera), basement block uplift (Frontal Cordillera), and adjacent hinterland basin (Iglesia-Calingasta basin); (2) a thin-skinned fold-thrust belt (Precordillera) with deformed basin fill exposed in intermontane valleys; (3) a proximal foreland basin (Bermejo basin) with a thick foredeep depocenter; and (4) a distal broken foreland partitioned by basement-cored block uplifts (Sierras Pampeanas).

The Principal Cordillera along the Chile-Argentina border (Figure 2a) consists of magmatic arc rocks and Mesozoic backarc basin strata that overlie Carboniferous-Triassic igneous rocks of the Choiyoi Group (Charrier et al., 2015; Cristallini & Ramos, 2000; Kay et al., 1989; Mackaman-Lofland et al., 2019). The Frontal Cordillera consist of a series of basemen-involved uplifts that exhume >3 km thick assemblage of Carboniferous-Triassic igneous rocks, (including the Elqui-Limarí and Chollay batholiths, and Choiyoi Group granodiorites, andesitic/rhyolitic lavas, and pyroclastic rocks), capped by Neogene volcanic and volcaniclastic rocks from the Andean arc (Coira et al., 1982; Heredia et al., 2002; Hervé et al., 2014; Kleiman & Japas, 2009; Mpodozis & Kay, 1992). The Principal and Frontal Cordilleras delivered sediments to the high elevation (~2,000 m) Iglesia-Calingasta-Uspallata basin (Figure 2b), which contains Neogene alluvial fan, fluvial, and lacustrine facies (Beer et al., 1990; Ruskin & Jordan, 2007; Val et al., 2016).

The Iglesia-Calingasta-Uspallata basin is separated from the eastern foreland by the Precordillera thrust belt, which deforms a >6 km thick Cambrian-Carboniferous succession of sedimentary marine deposits (Figure 2a; Ramos, 1999; von Gosen, 1992). More than 100 km of E-W shortening in the Precordillera was accommodated by imbricate thrusting above an ~4–12 km deep décollement (Allmendinger &

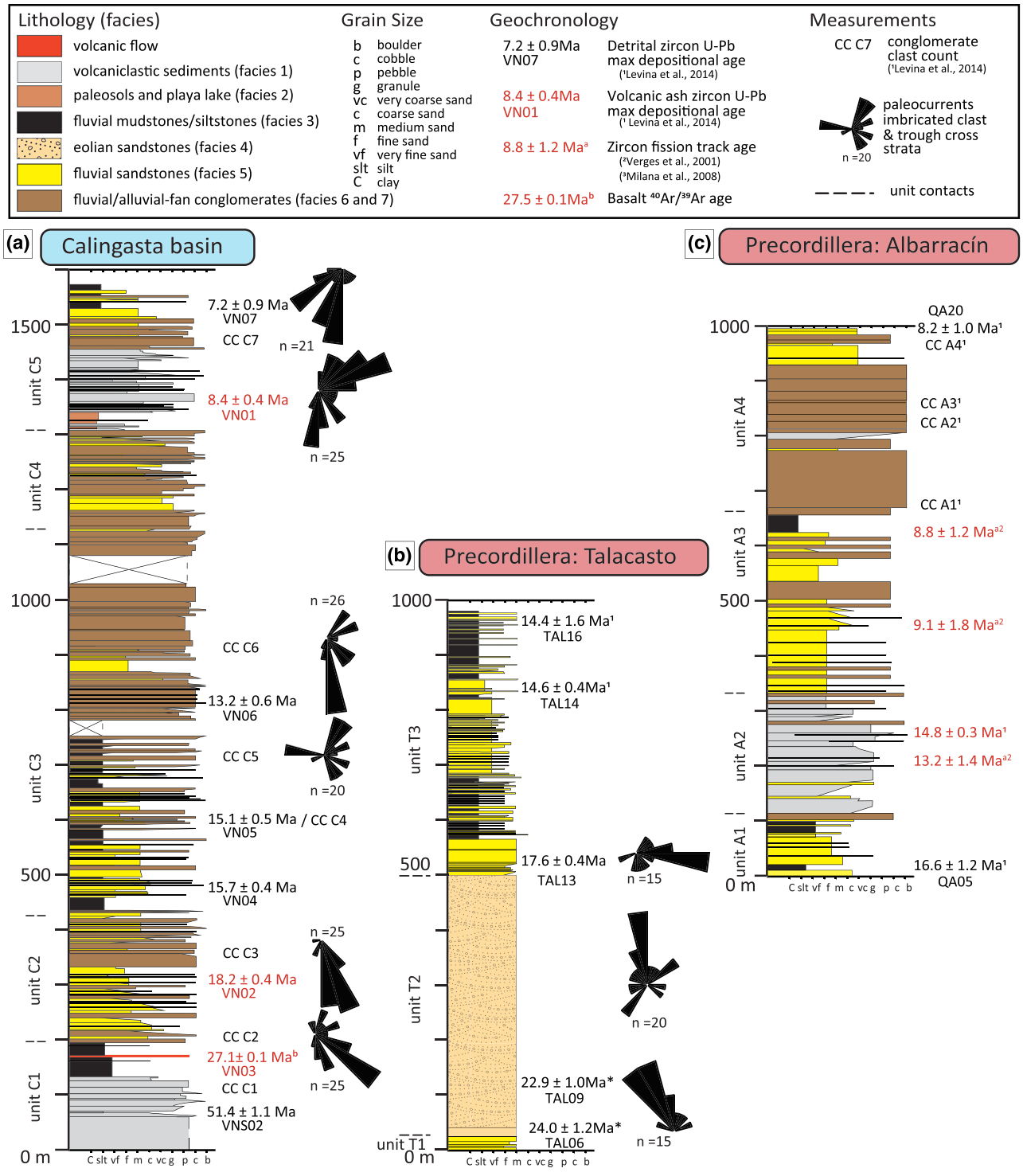

Figure 3. Stratigraphic sections from Argentina retroarc basins, location of rock samples and associated depositional age, paleocurrent measurements (rose diagrams), and clast count sites (CC). (a) Calingasta basin, Villa Nueva measured section. (b) Precordillera basin, Talacasto section (modified from Levina et al., 2014). (c) Precordillera basin, Albarracín section (modified from Vergés et al., 2001; Levina et al., 2014). (d) Proximal Bermejo basin, Mogna section (modified from Milana et al., 2003). (e) Distal Bermejo basin, Sierra Pie de Palo measured section. See Figure 2 for locations.

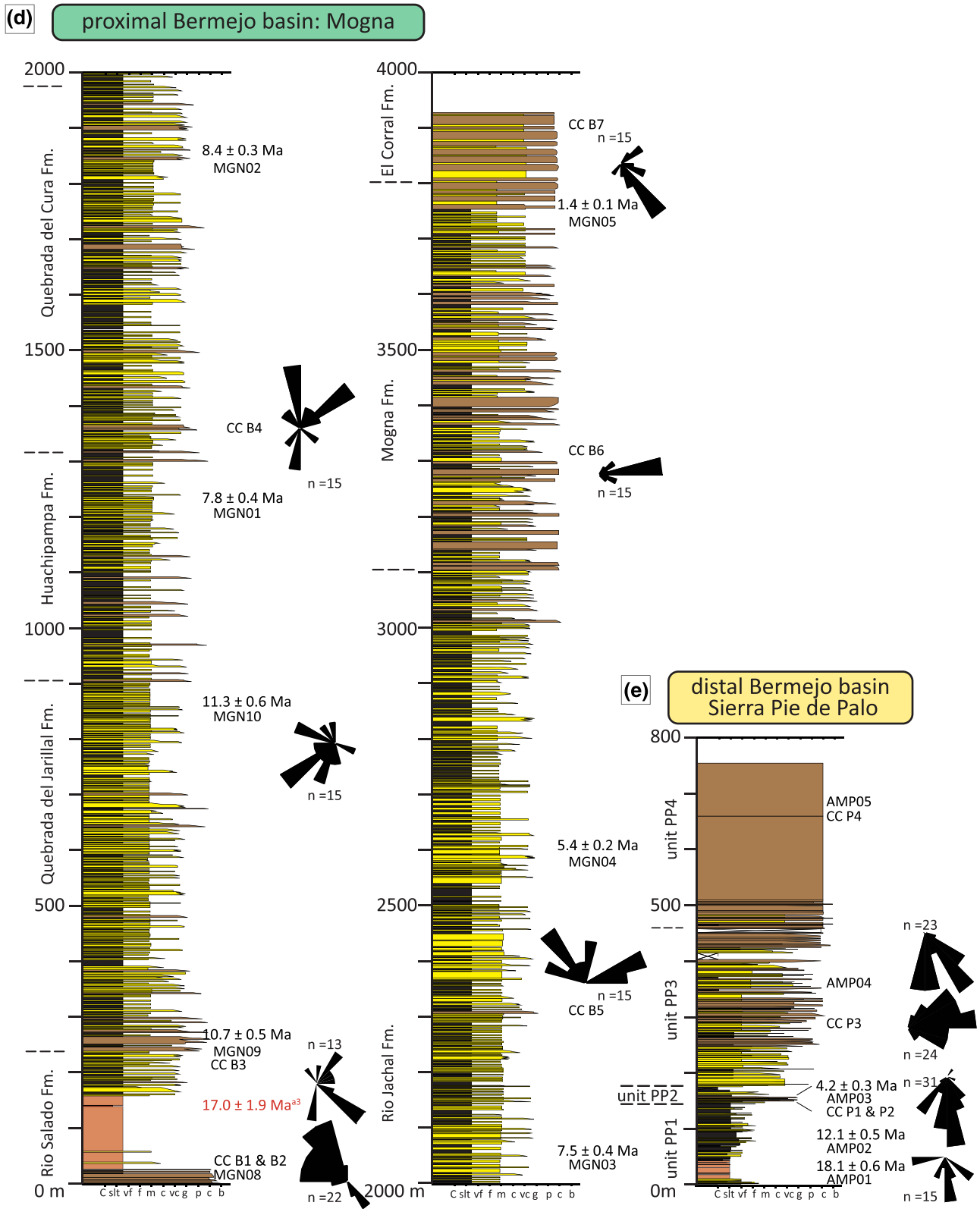

Figure 3. (continued)

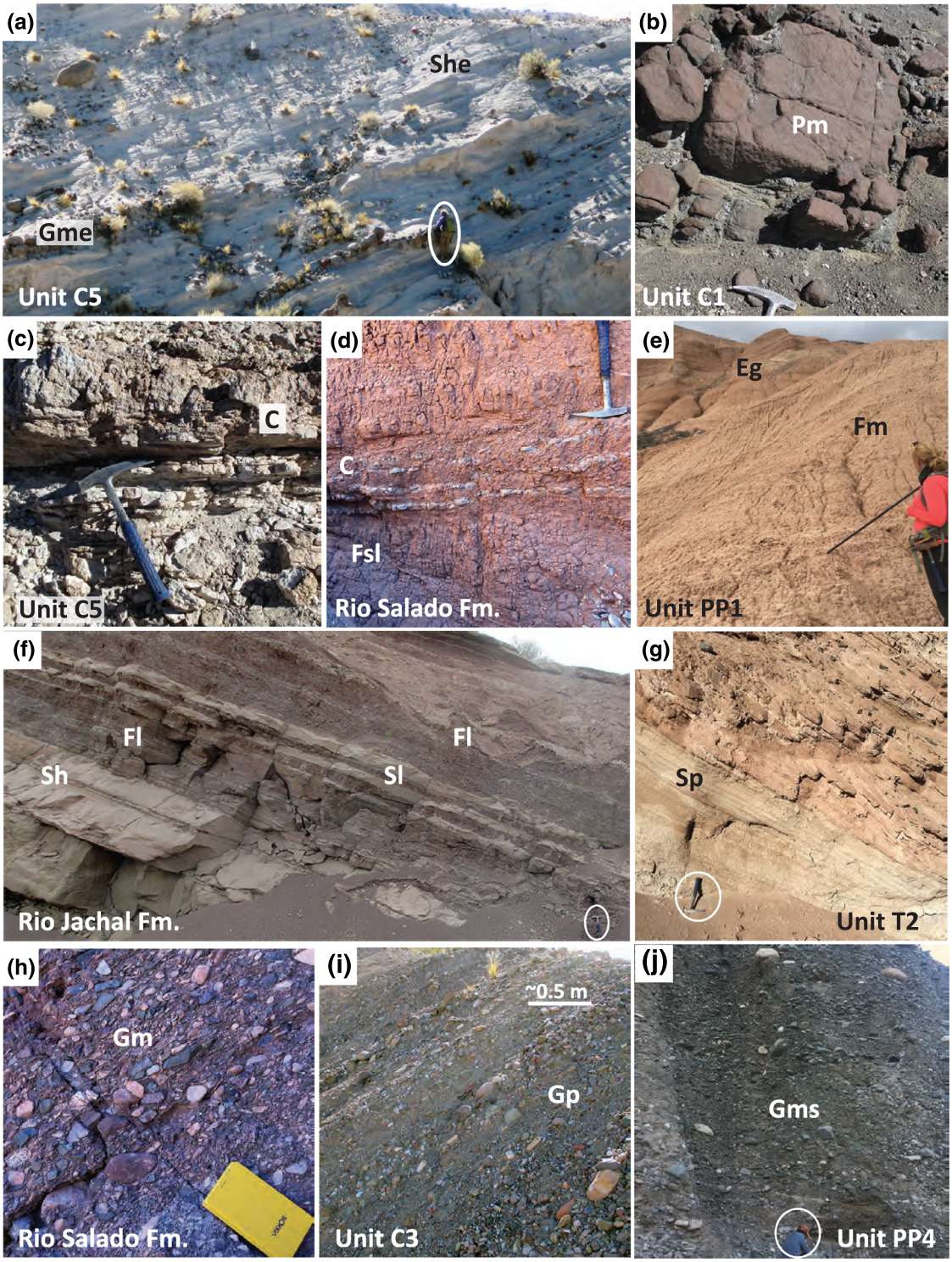

Figure 4. Field photographs of sedimentary deposits of the Calingasta, Precordillera, and Bermejo sections. (a) Volcaniclastic sequence of pebble-boulder conglomerates (lithofacies Gme) and medium-coarse tuffaceous sandstone (She) in Unit C5, Calingasta section. (b) Basalt flow sample VN03 in Unit C1, Calingasta section. (c) Interbedded carbonates and laminated calcareous siltstones (C) in lower Unit C5, Calingasta section. (d) Laminated mudstones (Fsl) and carbonates (C) in upper Rio Salado Formation, Mogna section. (e) Weakly bedded to structureless mudstones (Fm) and gypsum beds (Eg) lower Unit PP1, Sierra Pie de Palo section. (f) Amalgamated sand channels (Sh), laterally continuous thin, lenticular sand bodies (Sl), and interbedded laminated siltstones and mudstones (Fl) Rio Jachal Formation, Mogna section. (g) Large planar cross-stratified eolian sandstones (Sp) unit T2, Talacasto section. (h) Imbricated, gravel-cobble conglomerate (Gm) of metamorphic clast in lower Rio Salado Formation, Mogna section. (i) Cross-stratification conglomerates (Gp) in Unit C3, Calingasta section. (j) Matrix supported, poorly sorted cobble-boulder conglomerate (Gms) in unit PP4, Sierra Pie de Palo section.

Judge, 2014; Cristallini & Ramos, 2000; Fosdick et al., 2015; von Gosen, 1992). Within the Precordillera, Neogene fill preserved in the footwalls of major thrust faults (Talacasto and Albaracín valleys; Figure 2b) was part of a continuous foreland basin prior to late Miocene deformation (Figure 2b; Levina et al., 2014; Vergés et al., 2001). Preferential erosion formed intermontane valleys between thrust-generated ranges, such that north and south flowing tributary streams transport sediment downslope to east flowing transverse rivers that reach the modern foreland (Capaldi et al., 2017).

The proximal Bermejo foreland basin along the eastern flank of the Precordillera contains a thick, principally Miocene foredeep succession of fluvial and alluvial fan deposits (Figure 2; Irigoyen et al., 2000; Johnson et al., 1986; Jordan et al., 1992, 2001); Reynolds et al., 1990. Active sedimentation is dominated by fluvial megafans fed by large catchment areas (>10,000 km^2) with focused entry points into the proximal basin (e.g., Damanti, 1993; DeCelles & Cavazza, 1999; Horton & DeCelles, 2001). Bermejo strata crop out in west vergent backthrust structures along the eastern front of the Precordillera (e.g., Mogna section; Figure 2b; Milana et al., 2003; Zapata & Allmendinger, 1996).

Farther east, the distal Bermejo basin is disrupted by the Sierras Pampeanas, a series of roughly N trending basement uplifts (Figure 2a; González Bonorino, 1950; Jordan & Allmendinger, 1986; Stevens-Goddard et al., 2018). This broken foreland province is composed of metamorphic and igneous rocks exposed along the Sierra de Valle Fértil and Sierra Pie de Palo at 30–32°S (Figure 2a; Mulcahy et al., 2014; Ortiz et al., 2015). Precambrian-Ordovician igneous and metamorphic rocks are preserved across the Sierras Pampeanas and attributed to Pampean (555–515 Ma) and Famatinian (495–460 Ma) orogenesis, during accretion of Laurentian (i.e., Cuyania, and Pampia/MARA) terranes to the Gondwanan margin (Ducea et al., 2010; Ramos, 2004; Rapela et al., 2016; Schwartz et al., 2008; Thomas et al., 2015). On the eastern flank of the Sierra Pie de Palo, complex west vergent upper-crust structures kinematically linked to deeper east vergent basement structures (Bellahsen et al., 2016) expose Neogene basin fill that is capped by modern range-front alluvial fans (Figure 2b; Cuerda et al., 1983).

3. Depositional Systems

To assess depositional processes and environments, sedimentary facies associations were described for a 1,580 m thick composite stratigraphic section measured in two localities near Villa Nueva in the Calingasta basin (Figures 2b and 3a), and an ~750 m thick section in the distal, eastern Bermejo foreland basin within the Sierras Pampeanas province (Sierra Pie de Palo, Figures 2b and 3e). To enable a regional west-east comparison, these new sections are compared to Talacasto and Albarracín basin fill in the Precordillera (Figures 2, 3b, and 3c; Levina et al., 2014; Vergés et al., 2001), and Bermejo foredeep deposits in Mogna anticline (Figures 2 and 3d; Milana et al., 2003). Facies interpretations are presented here (Figure 4; Table 1, including individual lithofacies codes), and later incorporated into a basin-wide depositional synthesis (section 7).

3.1. Facies Associations

3.1.1. Facies 1: Volcanic and Volcaniclastic Deposits

Facies 1 includes gray to tan tuffs, sandstones, and conglomerates common in Calingasta units C1 and C5 and Precordillera Albarracín Unit A2 (Figures 3a and 3c). Finer facies include thin-bedded, nonwelded ash to lapilli tuffs that are poorly sorted, structureless to weakly stratified and laterally continuous over >10 m (lithofacies Pm). The ash and lapilli tuffs represent pyroclastic surge and intermittent fallout deposits derived from igneous centers (Cole & Decelles, 1991; Vergés et al., 2001). Coarser varieties include 0.5–2.25 m thick, matrix (ash) and clast supported pebble-boulder conglomerates with planar bases (Gme), and interbedded tabular to lenticular beds of horizontally stratified medium-coarse tuffaceous sandstones (She) with basal basaltic-andesite boulder lags (Figure 4a). These deposits are interpreted as debris flows to hyperconcentrated sheet flows deposited during lahar transport and/or fluvial reworking (Manville et al., 2009; Smith & Lowe, 1991). In the basal Calingasta succession, unit C1 contains a 5 m thick, vesicular andesitic-basalt with a red, oxidized lower contact (Figure 4b). The presence of a baked soil horizon suggests emplacement as a volcanic basalt flow during early Calingasta basin filling.

3.1.2. Facies 2: Lacustrine and Pedogenic Deposits

Facies 2 in Calingasta unit C5 is a laterally continuous (>5 km), resistant 5 m interval of white carbonates and laminated calcareous siltstone (lithofacies C) with abundant woody organic material (Figure 4c). The

Table 1
Facies and Interpretations for Calingasta, Precordillera, and Bermejo Basin Deposits

Facies	Lithofacies	Description	Occurrence	Interpretation
1	Gme, She, Pm	Buff-white to gray planar laminated matrix supported pebble to boulder conglomerate tuffs. Medium-coarse tuffaceous sandstones. Laterally continuous thin-bedded ash to lapilli tuffs. Primary volcanic flows.	Units C1, C5, PP2 and Huachipampa Fm.	Volcanic flow, surge, fall, and epiclastic deposits
2	C, Fsl, P, Eg	Buff white, tabular bedded carbonates and laminated to wavy calcareous siltstones, and reddish maroon, laminated muds, siltstones, and gypsum with desiccation cracks and carbonate concretions.	Units C1, C5, PP1; Rio Salado, Huachipampa, Quebrada del Cura, and Que-brada del Jarillal Fms.	Playa lake and Paleosol deposits
3	Sl, Sr, Fl, Fm, Fr	Tan-red-green planar to ripple cross-laminated mudstones and siltstones with common bioturbated and root traces. Thin laterally continuous tabular sandstone interbeds.	Units C5, T3 and PP1, Huachipampa, Quebrada del Cura, and Rio Jachal Fm.	Floodplain and Crevasse splay deposits
4	Sp, St, Sr	Maroon-tan, pink, and green thick sandstone deposits with large-scale cross stratification.	Unit T1 and T2	Eolian deposits
5	St, Sp, Sh, Se	Tan sandstone beds that are commonly amalgamated up to 15 m thick. Beds are massive, cross-bedded or planar bounded by low-relief erosive bases with intraclast, soft sediment deformation, and dewatering structures.	Quebrada del Jarillal, Quebrada del Cura, and Rio Jachal Fms.	Sandy fluvial channel deposits
6	Gm, Gt, Gp, Sh	Brown-gray pebble to cobble conglomerate that are moderately well sorted with imbricated, rounded clasts upward fining into large-scale sets of cross-bedded conglomerates and coarse sandstones with capping sandy-silt.	Units C2, C3, PP3, L and U Rio Salado, and Mogna Fms.	Braided river channel deposits
7	Gm, Gms	Clast to matrix supported, poorly sorted, cobble to boulder conglomerates.	Unit PP4 and El Corral Fm.	Debris flow deposits on alluvial fan

freshwater limestones contain coated grains and plant matter consistent with carbonate or tufa precipitation in a shallow pond or lake, possibly in an overbank fluvial setting (Capezzuoli et al., 2014; Horton & Schmitt, 1996; Marenssi et al., 2020). In the basal Bermejo basin (Rio Salado Formation and unit PP1), Facies 2 includes laminated red/maroon mudstones (Fsl), interbedded with thin, light green to white stromatolitic carbonates (Figure 4d; Cuerda et al., 1983; Milana et al., 2003). Bioturbated structureless mudstones to silty sandstones (Fm) with root traces (Fr) and desiccation cracks are associated with abundant gypsum intervals (Eg), and carbonate nodules (P). Facies 2 is attributed to deposition and pedogenesis in evaporative playa lake and distal overbank fluvial environments in a semi-arid system (DeCelles et al., 2015; Fosdick et al., 2017; Marenssi et al., 2020; Milana, 1991; Milana et al., 2003; Pietras & Carroll, 2006).

3.1.3. Facies 3: Fluvial Overbank Deposits

Facies 3 consists of 0.1–15 m thick packages of tan-red-green laminated mudstones and siltstones (lithofacies Fl) with interbedded 0.1–0.5 m thick, tabular fine sandstones with low angle (Sl) and ripple cross lamination (Sr) (Figure 4e). This facies represents fine-grained deposition from suspension or weak traction currents in an overbank fluvial setting, with thicker sand packages deposited by crevasse splays, and minor pedogenic modification (Burns et al., 2017; Horton & DeCelles, 2001; Levina et al., 2014; Miall, 1992).

3.1.4. Facies 4: Eolian Deposits

Facies 4 distinguishes the basal Talacasto unit T2 (Figure 3b), with very thick (~1–10 m) beds of maroon-tan, pink, and green fine- to medium-grained sandstones containing large-scale cross-stratified beds (lithofacies Sp) that commonly preserve low-angle, tangential bases (St) and subordinate thin (0.5–30 cm) beds of ripple cross stratified (Sr) and structureless sandstones (Figure 4g). Thin dark red, horizontally laminated siltstones and mudstones are locally preserved. Bounding surfaces between thick sandstone units vary between extensive low-angle planar to locally scalloped bedding surfaces. The thick cross-stratified sandstones are interpreted as eolian dune deposits containing foresets generated by grain flow and wind ripple modification; thin-bedded siltstones represent interdune deposition (Levina et al., 2014; Tripaldi & Limarino, 2005).

3.1.5. Facies 5: Sandy Fluvial Channel Deposits

Facies 5 represents tan fine- to medium-grained 0.8–4 m thick sandstone beds that are commonly stacked vertically and shingled in laterally continuous sheets up to 15 m thick. Sedimentary structures include trough (lithofacies St) and planar cross stratification (Sp), horizontally stratified beds (Sh) bounded by

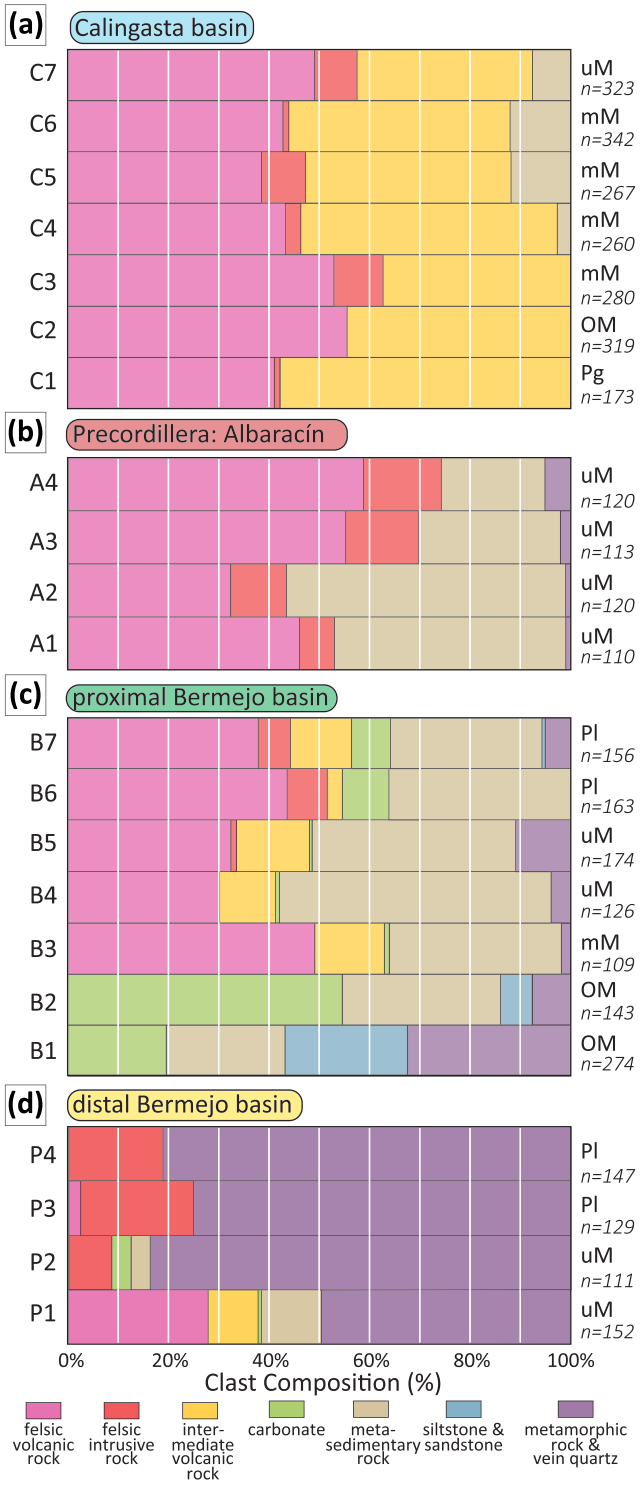

Figure 5. Plot of conglomerate clast compositions based on seven lithologic categories for the retroarc basin system: (a) Calingasta basin; (b) Precordillera Albarracín section; (c) proximal Bermejo basin (Mogna); (d) distal Bermejo basin (Sierra Pie de Palo). Conglomerate age labeled as Paleogene (Pg), Oligocene-Miocene (OM), middle-Miocene (mM), upper-Miocene (uM), Pliocene-Modern (Pl). See Figure 3 for clast count localities.

low-relief erosive bases with mudstone rip-up clast (Se), soft sediment deformation, and dewatering structures (Figure 4f). These sandstone packages are interpreted as the product of sand deposition within bank-attached and in-channel bars in a braided fluvial system (Lawton et al., 2014; Limarino, et al., 2001). Interbedded finer materials suggest periodic development and collapse of channel-margin levees, such that unstable distributive channels commonly avulsed onto adjacent floodplains (e.g., DeCelles & Cavazza, 1999; Horton & DeCelles, 2001).

3.1.6. Facies 6: Gravely Braided Fluvial Deposits

Facies 6 constitutes brown, pebble-cobble conglomerates that are moderately well sorted with imbricated, rounded clasts (lithofacies Gm). Stacked conglomerate beds form 2–12 m thick upward fining sequences with a thin (<0.25 m) lag of massive conglomerate that passes upward into planar to trough cross-stratified conglomerates (lithofacies Gt, Gp) and structureless to horizontally stratified coarse sandstones (Sh) with capping sandy-siltstones (Figures 4h and 4i). Facies 6 is interpreted as a braided fluvial system with migration of transverse and longitudinal gravel bars (Miall, 1977, 1985).

3.1.7. Facies 7: Debris Flow Deposits

Facies 7 in upper Bermejo, and Precordillera Albarracín basin fill (Figures 3c–3e) consists of structureless to poorly stratified, very poorly sorted, cobble-boulder conglomerates that are clast or matrix supported (lithofacies Gms, Gm), with subangular and sharp nonerosive bases (Figure 4j). Bed thicknesses range from 0.5 to 3 m and exhibit weak normal to inverse grading, with tabular to lenticular beds of planar cross-stratified coarse sandstone (Sp). These facies are interpreted as gravelly debris flows and late-stage sandy hyperconcentrated flows on an alluvial fan (Horton & Schmitt, 1996; Nemec & Steel, 1984; Perez & Horton, 2014).

3.2. Paleocurrents

Paleocurrent measurements help constrain sediment dispersal patterns across the retroarc basin system. At 20 localities, flow directions were determined from at least 20 imbricated clasts or 15 trough limbs (Figure 3). Measurements were corrected for bedding dip and azimuthal flow directions were calculated (Table S1 in the supporting information). Throughout the Calingasta basin, imbricated clasts show fluvial sediment dispersal toward the south and southeast (Figure 3a). In the Precordillera, eolian cross-strata in lower stratigraphic levels show foreset orientations consistent with NNW migrating transverse dunes (Figure 3b). An upsection shift to fluvial deposition is accompanied by a shift to east directed flow (Figure 3b), similar to the Precordillera Albarracín section (Vergés et al., 2001). In the proximal Bermejo basin (Mogna), clast imbrication in the basal Rio Salado Formation indicates NW directed flow. Upsection, fluvial trough-cross strata of the Rio Salado Formation show broadly eastward flow, whereas imbricated clasts in the Mogna and El Corral Formations indicate ESE flow (Figure 3d). In the distal Bermejo basin (Sierra Pie de Palo), south directed flow for lower levels shifts to ESE flow in upper levels (Figure 3e).

3.3. Conglomerate Clast Compositions

Pebble-boulder clast compositional data were collected at 18 sites in the Calingasta and Bermejo (Mogna and Sierra Pie de Palo) sections (Figure 5; supporting information Table S2) and compared to clast

lithologies from the Albarracín section (Levina et al., 2014; Vergés et al., 2001). Clasts were grouped into seven categories: (1) felsic volcanic rocks of Permian-Triassic rhyolite suite; (2) granite and diorite of Carboniferous-Triassic and Cenozoic magmatic arc rocks; (3) fine-grained mafic to porphyritic intermediate volcanic rocks of the Cenozoic magmatic arc; (4) green to tan metamorphosed sandstone and siltstone from Silurian-Devonian strata; (5) red to brown siltstone and sandstone from Carboniferous-Triassic strata; (6) carbonate and chert from Cambrian-Ordovician units; and (7) metamorphic lithologies including amphibolitic gneiss, schist, marble, and vein quartz from Precambrian-Ordovician basement.

Calingasta clast counts (C1–C7) display a bimodal distribution of felsic and intermediate volcanic rocks with the appearance of metasedimentary lithologies (C4) in middle Miocene levels (Figure 5a). Precordillera clast counts from the Albarracín section display Paleozoic metasedimentary clasts with an increased felsic volcanic clasts in upper Miocene strata (Figure 5b; Levina et al., 2014; Vergés et al., 2001). In the proximal Bermejo Basin, the lower Rio Salado Formation (B1, B2) exhibits mixed metamorphic (32%), sandstone (24%), metasedimentary (23%), and carbonate (19%) lithologies. In the middle to upper Miocene Quebrada del Jarillal, Huachipampa, Quebrada del Cura and Rio Jachal Formations (B3–B5), a bimodal distribution of metasedimentary (34–54%) and felsic volcanic (30–49%) clasts is supplemented by intermediate/mafic volcanics (11–14%) and vein quartz (2–11%) lithologies (Figure 5c). The Pliocene Mogna and El Corral Formations (B6-B7) exhibit felsic volcanic (38–44%), metasedimentary (30–36%), and minor carbonate (8–9%), felsic intrusive (6–8%), and intermediate volcanic (3–12%) clasts. In the distal Bermejo basin, felsic, and intermediate volcanic clasts (38%) in lower levels (P1) shift to igneous and metamorphic (>80%) lithologies (P2–P4) (Figure 5d).

4. Geochronology

4.1. Basalt $^{40}Ar/^{39}Ar$ Geochronology

An andesitic basalt flow (sample VN03; Figure 4b) was collected from the lowermost levels of the Calingasta basin (Unit C1). Basalt groundmass was concentrated by coarse crushing; fragments visibly free of phenocrysts were selected for 8 hr irradiation at the USGS TRIGA reactor in Denver, Colorado. The $^{40}Ar/^{39}Ar$ step-heating analyses were performed using a 55 W Photon-Machine diode laser and Helix multicollector plus mass spectrometer with an automated all-metal extraction system at the New Mexico Geochronology Research Laboratory (see supporting information Table S3).

The $^{40}Ar/^{39}Ar$ age spectrum displays an initial apparent age of ~40 Ma for the lowest temperature step with limited (<15%) gas release. The remaining 12 steps show a sharp decrease in apparent age, yielding consistent ages in the 26–30 Ma range. A uniform flat segment defined by the final seven steps yields a weighted mean plateau age of 27.05 ± 0.07 Ma. The first half of the K/Ca spectrum is typical of groundmass with values near 1 before diminishing to values near 0.1 for higher temperature steps. The isochron plot (Table S3) suggests excess argon for steps A-E with an initial $^{40}Ar/^{39}Ar$ trapped component of 312 ± 1 Ma and an isochron age of 27.5 ± 0.03 Ma that is near the weighted mean plateau age and the integrated (total gas) age of 27.65 ± 0.02 Ma (Table S3). Therefore, the initial old ages (>28 Ma) from the step-heat analyses are the probable result of excess argon, and the plateau age of 27.05 ± 0.07 Ma is considered to represent the basalt emplacement age.

4.2. Detrital Zircon U-Pb Geochronology

U-Pb analyses were conducted on 19 Cenozoic sandstones, two ash fall tuffs, and one river sand sample from the retroarc basin system (Figure 3 and Table S4). Mineral separation included crushing, grinding, and water table, heavy-liquid density, and magnetic susceptibility separations. Nonmagnetic heavy mineral separates were poured onto double sided tape on 2.5 cm epoxy resin mounts, then zircon grains were chosen randomly for analysis by laser ablation-inductively coupled plasma-mass spectrometry (LA-ICP-MS) to obtain zircon U-Pb ages. At least 120 analyses per sandstone and ~30 analyses for volcanic samples were carried out on individual zircon grains free of fractures and inclusions. Sample mounts were loaded into a large-volume Helex sample cell and analyzed with a single-collector, magnetic sector Element 2 ICP-MS with a PhotonMachine Analyte G.2 excimer laser (Horton et al., 2016; Odlum et al., 2019). Corrections for depth-dependent, elemental and isotopic fractionation were performed using zircon standard GJ1

(600.4 ± 0.1 Ma; Jackson et al., 2004) and secondary standards Plesovice (PL-1; 337.2 ± 0.4 Ma; Sláma et al., 2008) and 91,500 (1065 Ma; Wiedenbeck et al., 1995).

Zircon U-Pb ages and 2σ errors are reported for analyses with <10% $^{206}Pb/^{238}U$ uncertainties, <20% discordance, and <5% reverse discordance. Reported values for grains <850 Ma are $^{206}Pb/^{238}U$ ages with $^{206}Pb/^{238}U$ versus $^{207}Pb/^{235}U$ discordance, whereas values for grains >850 Ma ages are $^{207}Pb/^{206}Pb$ ages with $^{206}Pb/^{238}U$ versus $^{207}Pb/^{206}Pb$ discordance. Discordance filters for Miocene zircons (<23 Ma) were expanded to incorporate ages with <20% $^{206}Pb/^{238}U$ uncertainties and <50% discordance $^{206}Pb/^{238}U$inorder to prevent biasing due to exclusion of young grains with higher ^{207}Pb and associated calculated $^{207}Pb/^{235}U$ ages that are systematically older than measured $^{206}Pb/^{238}U$ ages (Table S4). U-Pb results for individual samples are arranged in stratigraphic order and displayed as probability density plots (PDPs) with histogram age bins (Figures 6–8). Cenozoic to Neoproterozoic ages (0–1500 Ma) dominate the zircon age distributions. Results for Neogene samples are displayed as probability density functions from 0 to 66 Ma with 5 Myr histogram age bins to identify potential syndepositional ages and Andean magmatic age components, whereas ages from 200 to 1500 Ma are plotted with 25 Myr histogram age bins.

4.2.1. Maximum Depositional Ages

A maximum depositional age for the 19 sandstone samples and two tuff samples was derived from the calculated weighted mean age of the youngest grain cluster overlapping by 2σ concordant U-Pb ages (following approaches established by Dickinson & Gehrels, 2009; Coutts et al., 2019). In cases where two or more grains do not overlap by 2σ, the youngest single grain was selected as the maximum depositional age (Table S5) and plotted at the corresponding stratigraphic level (Figure 3).

Most Cenozoic sandstone samples contain young age populations broadly consistent with previous age assessments (Levina et al., 2014; Milana et al., 2003; Vergés et al., 2001), with the exception of sample MGN08 from lower Rio Salado Formation conglomerates in Bermejo Foreland section (Figure 3d) and samples AMP04 and AMP05 from units PP3 and PP4 in the Sierra Pie de Palo section (Figure 3e). Moreover, the results from sandstone samples are consistent with the depositional ages determined for volcanic samples in this study: 18.2 ± 0.4 Ma (VN02) and 8.4 ± 0.4 Ma (VN01) (Figure 3). Collectively, samples across the retroarc basin system show a systematic upsection decrease in maximum depositional age, with the exception of samples MGN10 (11.3 ± 0.6 Ma) and MGN02 (7.8 ± 0.4 Ma) in the Bermejo section (Figure 3d). On the basis of the internal consistency, stratigraphic coherence, and concordance with volcanic ages, the calculated maximum depositional ages are regarded as viable approximations of stratigraphic age.

4.3. Source Characterization Using Modern River Detrital Zircons

Detrital zircon (DZ) U-Pb analyses of modern river sands help define regional magmatic and metamorphic histories (Ducea et al., 2018; Finzel, 2019; Link et al., 2005; Pepper et al., 2016) and identify the impact of erosion, zircon fertility, and lithologic erodibility on provenance signatures (e.g., Amidon et al., 2005; Horton et al., 2015; Jackson et al., 2019; Malkowski et al., 2020). Zircon U-Pb ages for Andean rivers draining the Principal Cordillera, Frontal Cordillera, Precordillera, and Sierras Pampeanas (Capaldi et al., 2017, 2019) help characterize provenance variations across hinterland, wedge-top, foreland, and broken foreland basin settings (Figure 6), providing an opportunity to track Cenozoic erosional unroofing and sediment routing patterns.

4.3.1. Principal Cordillera

Modern river sands near the Chile-Argentina border yield major Andean arc (201–0 Ma) and minor Cordillera (350–225 Ma) age groups (Figure 6a). Jurassic to Paleogene DZ ages are consistent with erosion of the Andean magmatic arc, including the Coastal Cordillera, and volcanic and sedimentary rocks of the Principal Cordillera (Figure 2a; Kay et al., 2005; Mackaman-Lofland et al., 2019; Parada et al., 1999).

4.3.2. Frontal Cordillera

Frontal Cordillera river sands exhibit Permian-Triassic (280–225 Ma), Carboniferous (350–280 Ma), and subordinate Neogene (<23 Ma) age components (Figure 6b). Carboniferous-Permian arc rocks (350–280 Ma), Choiyoi igneous rocks (280–240 Ma), and Triassic plutons are the main rock units in the Frontal Cordillera (del Rey et al., 2016; Mpodozis & Kay, 1992). Miocene to Quaternary (23–0 Ma) zircons from Andean arc rocks and recycled volcaniclastic rocks across the Frontal Cordillera (Figure 2a; Jones et al., 2015; Kay et al., 1991; Kay & Mpodozis, 2001). Predicted provenance variations associated with orogenic unroofing along Frontal Cordillera structures involves initial erosion of Neogene volcanic and volcaniclastic cover

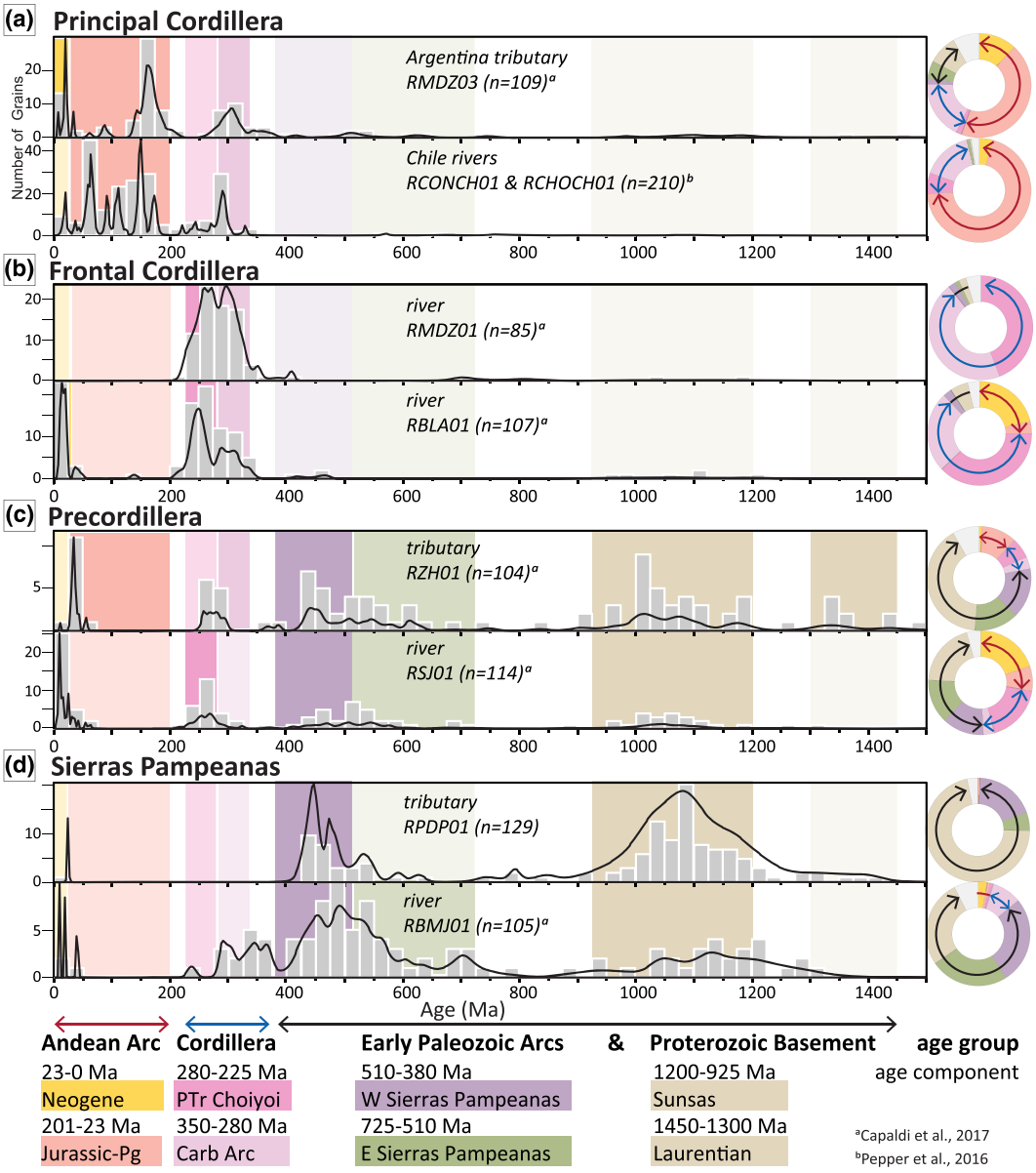

Figure 6. Comparative plot of detrital zircon U-Pb age distributions for modern river sands, depicted as relative probability density curves and age histograms, with emphasis on key age components (color shading). Ring diagrams at right represent the relative abundance of key age components (color shading) and age groups: Andean arc (red arrow), Cordillera (blue arrow), and Proterozoic-lower Paleozoic basement (black arrow) for each sample. (a) Principal cordillera rivers. (b) Frontal cordillera rivers. (c) Precordillera rivers. (d) Sierras Pampeanas rivers. Data sources: (a) Capaldi et al. (2017); (b) Pepper et al. (2016).

(RBLA01) followed by increased contributions from Carboniferous to Triassic igneous rocks (RMDZ01) (Figure 6b; Mackaman-Lofland et al., 2020; Pinto et al., 2018).

4.3.3. Precordillera

In the Precordillera, the main trunk river (RSJ01) shows multimodal DZ age distributions with Andean arc (<23 Ma), Permian-Triassic (280–225 Ma), western Sierras Pampeanas (510–380 Ma), eastern Sierras Pampeanas (725–510 Ma), and Sunsas (1200–925 Ma) age components (Figure 6c). Small intermontane axial tributaries (RZH01) display significantly older ages, including Laurentian (1450–1300 Ma) age components. Precordilleran river sand age distributions derive from the Mesozoic-Cenozoic Andean Arc (<201 Ma) and Paleozoic Cordilleran (350–225 Ma) age groups that represent sediment recycled from exhumed Neogene basin fill (Figure 2a). The presence of older ages (>380 Ma) is attributed to Paleozoic metasedimentary rocks in the Precordillera, with potential recycling from Neogene strata (Capaldi et al., 2017). Predicted

sedimentary unroofing sequence for Precordillera shortening involves initial erosion of Neogene basin strata (RSJ01) then into underlying Paleozoic metasedimentary sequence (RZH01) (Figure 6c; Fosdick et al., 2015; Suriano et al., 2017).

4.3.4. Sierras Pampeanas

Rivers in the eastern broken foreland tap Sierras Pampeanas uplifts that expose Carboniferous-Triassic strata and Precambrian-Ordovician igneous and metamorphic basement (Figure 2a). River sand DZ age distributions show western Sierras Pampeanas (510–380 Ma), eastern Sierras Pampeanas (725–510 Ma), and Sunsas (1200–925 Ma) age components with minor and Andean arc and Cordillera (<350 Ma) age groups (Figure 6d). Major basement sources include the western Sierras Pampeanas (510–380 Ma), Famatinian arc rocks (495–440 Ma), and metamorphic assemblages (460–385 Ma) (Mulcahy et al., 2014; Otamendi et al., 2017). The eastern Sierras Pampeanas includes a dominant 538–515 Ma age peak from Pampean arc magmatism and minor 725–540 Ma component from metasedimentary rocks (Puncoviscana Formation) (Rapela et al., 2007; Schwartz et al., 2008). Proterozoic basement ages (1450–925 Ma) have a dominant Sunsás (1200–925 Ma) cratonal age component and a minor Laurentian (1450–1300 Ma) age component from the Cuyania terrane underlying the western Sierras Pampeanas (Bahlburg et al., 2009; Chew et al., 2007; Ramos, 2004, 2009; Rapela et al., 2016). Recycled Proterozoic-early Paleozoic ages (>380 Ma) are common in Phanerozoic strata (Figure 6). The expected unroofing pattern in the Sierras Pampeanas involves erosion of Neogene and Mesozoic basin fills (RBMJ01) followed pre-Mesozoic basement rocks (RPDP01) (Figure 6d).

5. Provenance Synthesis

Paleocurrents, conglomerate clast compositions, and detrital zircon (DZ) U-Pb age distributions provide insights on Cenozoic unroofing patterns and sediment provenance for five basin localities: the Calingasta basin, Talacasto and Albarracín valleys of the Precordillera, and proximal (western) and distal (eastern) localities of Bermejo basin. Using river sand zircon U-Pb ages as a comparative baseline for each locality, we recognize the following steps in the evolution of the retroarc basin system (with DZ age distributions displayed in Figure 7): (1) Paleogene (>24 Ma) deposition during erosion of the Principal Cordillera; (2) latest Oligocene-early Miocene (24–17 Ma) Calingasta and Precordillera sedimentation fed by Principal Cordillera sources, and initial Bermejo basin accumulation of sediment from eastern cratonic regions; (3) middle Miocene (17–11 Ma) deposition during unroofing of the Frontal Cordillera; (4) late Miocene (11–5 Ma) accumulation in the Bermejo foreland with principally Precordillera sources; and (5) Pliocene to present (5–0 Ma) accumulation in a broken foreland province fed by Sierras Pampeanas basement uplifts.

5.1. Paleogene: Principal Cordillera Sources

Paleogene deposits are limited to the Calingasta basin (unit C1, VNS02; Figure 7a). Clast lithologies are principally (>50%) intermediate to mafic volcanic clasts, with basalts and andesites (Figure 5a). DZ age distributions are strongly bimodal with Cretaceous to Eocene, and Permian-Triassic (280–225 Ma) age components, comparable to modern rivers of the Principal Cordillera (Figure 6a). Interpreted sediment sources include western Andean arc volcanic deposits and/or recycled Principal Cordillera volcaniclastic basin fill (e.g., Cristo Rendentor Formation) (Figure 2b; Fosdick et al., 2017; Mackaman-Lofland et al., 2019). The Permian-Triassic age component likely reflects local input of Choiyoi volcanic rocks (Figure 2b).

5.2. Latest Oligocene-Early Miocene: Mixed Cordilleran and Cratonic Sources

Uppermost Oligocene-lower Miocene deposits exhibit two provenance signatures: western Cordilleran sources for proximal deposits and eastern cratonic sources for more-distal zones. Calingasta basin conglomerates show SE directed flow and bimodal felsic (55%) and intermediate (45%) volcanic clast lithologies. Coeval fluvial-eolian deposits in the Precordillera (Talacasto section) record broadly north directed paleowinds and dominantly Eocene-Oligocene (45–25 Ma) and Carboniferous-Permian (350–280 Ma) DZ age distributions (Figure 7b. TAL06&09). The overlying fluvial deposits (Talacasto unit T3) display an increased Miocene Andean arc (<23 Ma) age component (Figure 7b; TAL13). Talacasto age distributions are most similar to Principal Cordillera river sands (Figure 6a). These results show that the proximal (Calingasta and Precordillera) foreland basin was dominated by western sources, including Andean arc rocks of the Principal Cordillera (Mackaman-Lofland et al., 2020).

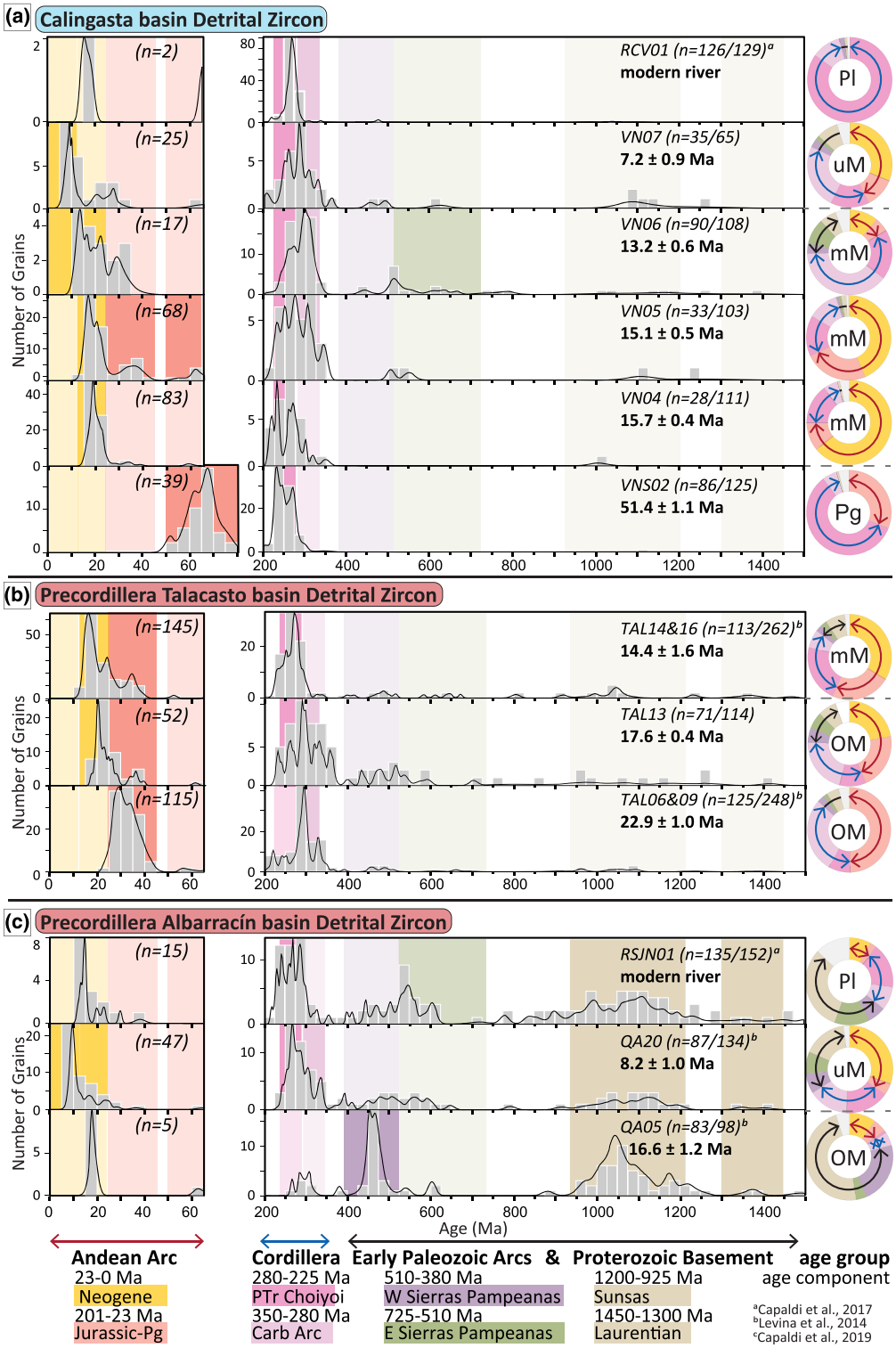

Figure 7. Comparative plot of detrital zircon U-Pb age distributions for sandstone samples, depicted as relative probability density curves and age histograms, with emphasis on key age components (color shading). Ring diagrams at right represent the relative abundance of key age components (color shading) and age groups: Andean arc (red arrow), Cordillera (blue arrow), and Proterozoic-lower Paleozoic basement (black arrow) for each sample. (a) Calingasta basin. (b) Precordillera Talacasto section. (c) Precordillera Albarracín section. (d) Proximal Bermejo basin samples. (e) Distal Bermejo basin samples. Inner ring labels correspond to sandstone sample age: Paleogene (Pg), Oligocene-Miocene (OM), middle-Miocene (mM), upper-Miocene (uM), Pliocene-Modern (Pl). Data sources: a (Capaldi et al., 2017); b (Levina et al., 2014); c (Capaldi et al., 2019).

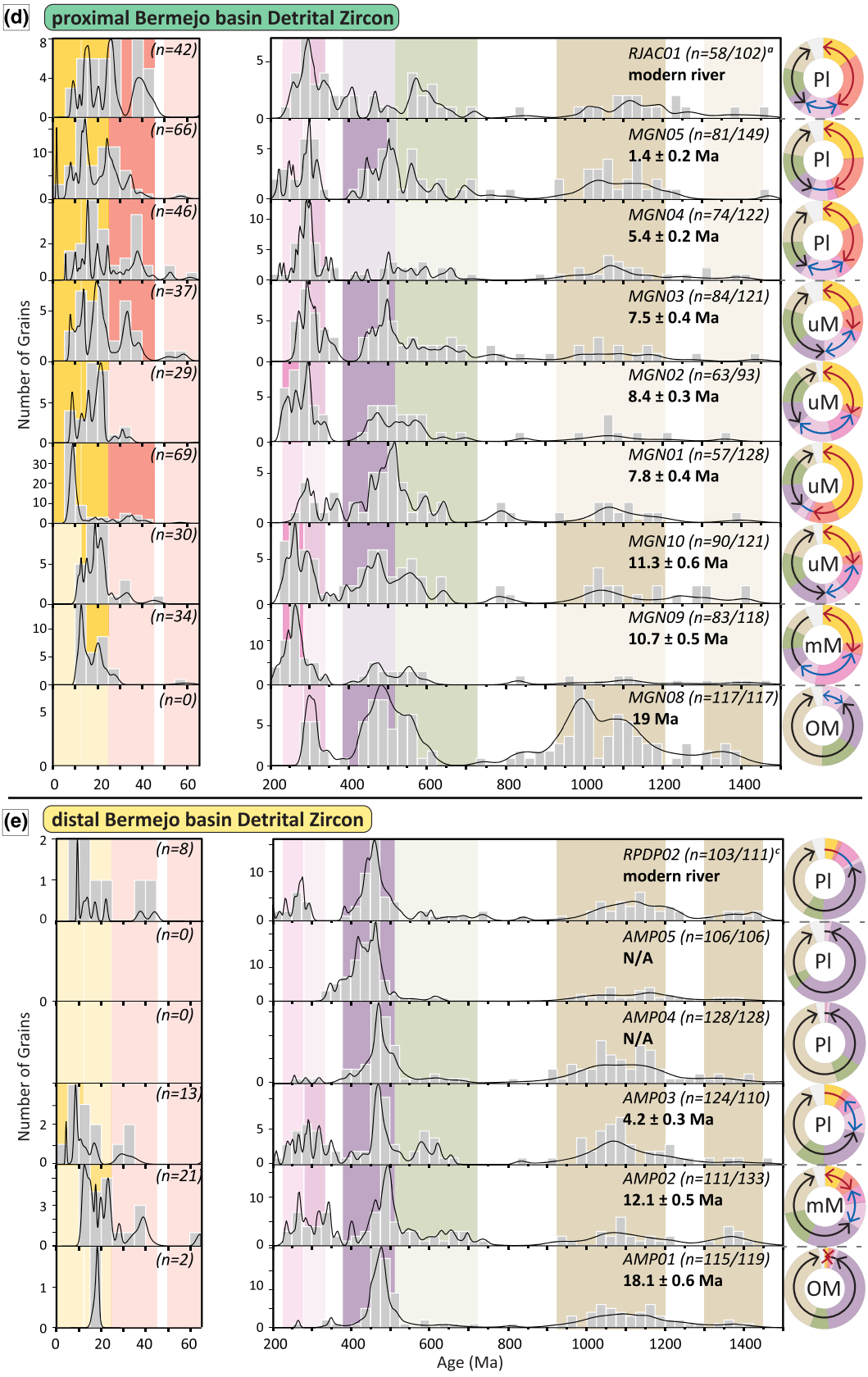

Figure 7. (continued)

In contrast, coeval strata in more distal (Albarracín and Bermejo) localities (Figures 7c–7e) recorded eastern cratonic sources. The Rio Salado Formation (western Bermejo basin) preserves NE directed sediment dispersal with carbonate, siliciclastic, metasedimentary, and metamorphic clasts (Figure 5c; B1, B2). DZ age distributions for Albarracín (Figure 7c; QA05) and Bermejo basin (Figure 7d; MGN08; Figure 7e; AMP01) localities are dominated by Proterozoic-lower Paleozoic basement (1450–380 Ma) ages, similar to modern river sands in the Sierras Pampeanas (Figure 6d). These results show that more-distal Oligocene-lower Miocene deposits were derived from eastern cratonic and overlying Paleozoic-Mesozoic strata.

5.3. Middle Miocene: Frontal Cordillera Hinterland Unroofing

Middle Miocene fluvial deposits recorded local derivation (Calingasta and Talacasto localities) from the Frontal Cordillera and subsequent advance of a broader Cordilleran signal across the foreland (Bermejo basin). Unroofing of the Frontal Cordillera is revealed by upsection shifts in DZ signatures within Calingasta unit C3 (Figure 7a: VN04, VN05, VN06) and Talacasto unit T3 (Figure 7b; TAL14, TAL16), with an enhanced Carboniferous-Permian (350–280 Ma) age component, uniform Permian-Triassic (280–225 Ma) ages, and diminished Neogene (<23 Ma) zircons from the Andean arc. Calingasta conglomerates are dominated by bimodal felsic to intermediate volcanic clasts, reflecting continued Frontal Cordillera input (Figure 5a; C4, C5, and C6). These trends suggest progressive exhumation of young Andean volcanic cover and then underlying Carboniferous -Triassic igneous units (Mackaman-Lofland et al., 2020; Pinto et al., 2018).

In the Bermejo basin middle Miocene deposits registered eastward dispersal and the arrival of volcanic detritus (Figure 6c; B3). Andean arc and Cordilleran (350–0 Ma) DZ age signatures appeared in both proximal (MGN09) and distal (AMP02) sectors of the Bermejo basin (Figures 9a and 9b). The middle Miocene arrival of Andean hinterland signatures across various basin segments indicates a regional shift to an integrated, expanded drainage network with enhanced distribution of Andean detritus to an extensive east flowing sediment routing system.

5.4. Late Miocene: Precordillera Thrust Belt Sources

Upper Miocene fluvial and alluvial fan conglomerates in proximal basin segments (Calingasta and Precordillera) show south and east directed flow with mixed volcanic and metasedimentary clast lithologies (Figures 5a and 5b; Levina et al., 2014; Vergés et al., 2001). DZ age distributions from Calingasta (Figure 7a; VN07) and Albarracín (Figure 7c; QA20) deposits reflect Andean arc (23–0 Ma), Permian-Triassic (280–225 Ma), and Carboniferous arc (350–280 Ma) age components, with minor Proterozoic-lower Paleozoic basement (>380 Ma) contributions. These match modern river age distributions in the Frontal Cordillera and Precordillera (Figures 6b and 6c).

Proximal Bermejo basin deposits DZ age distributions show all older age (>200 Ma) signatures and registered an upsection shift from syn-deposition (<10 Ma) to older (10–45 Ma) Cenozoic age populations (Figure 7d). These DZ age distributions are similar to Precordillera river and tributary sands (Figure 6c). The provenance trends likely represent shortening within the Precordillera thrust belt and associated erosional unroofing of recycled Cenozoic basin deposits and underlying Paleozoic metasedimentary rocks (Fosdick et al., 2015; Levina et al., 2014; Suriano et al., 2017).

5.5. Pliocene-Quaternary: Sierras Pampeanas Basement Exhumation

Pliocene fluvial and alluvial fan deposits in the proximal Bermejo basin show east directed flow with carbonate, volcanic, and metasedimentary clast lithologies (Figure 5b; B6, B7). Complex multimodal DZ age distributions indicate continued recycling of Cenozoic basin deposits, Precordillera, and Frontal Cordillera igneous rock sources (Figure 7d; Fosdick et al., 2015). Distal Bermejo basin alluvial fan deposits display ESE flow and enhanced (80–100%) metamorphic and intrusive igneous clast (Figure 5d). Sierras Pampeanas erosion is revealed by upsection shifts in DZ age distributions in units PP2-PP4 (AMP03-AMP05), with diminished Andean (<66 Ma) and Cordilleran (225–350 Ma) age components, and increased western Sierras Pampeanas (510–380 Ma) age component (Figure 7e). These provenance trends indicate exhumation of Sierra Pie de Palo basement block (Figure 2a).

By comparison, a modern river sand sample from the Calingasta basin (Figure 7a; RCV01) displays a unimodal Permian-Triassic (280–225 Ma) age component indicating further exhumation of the Frontal Cordillera

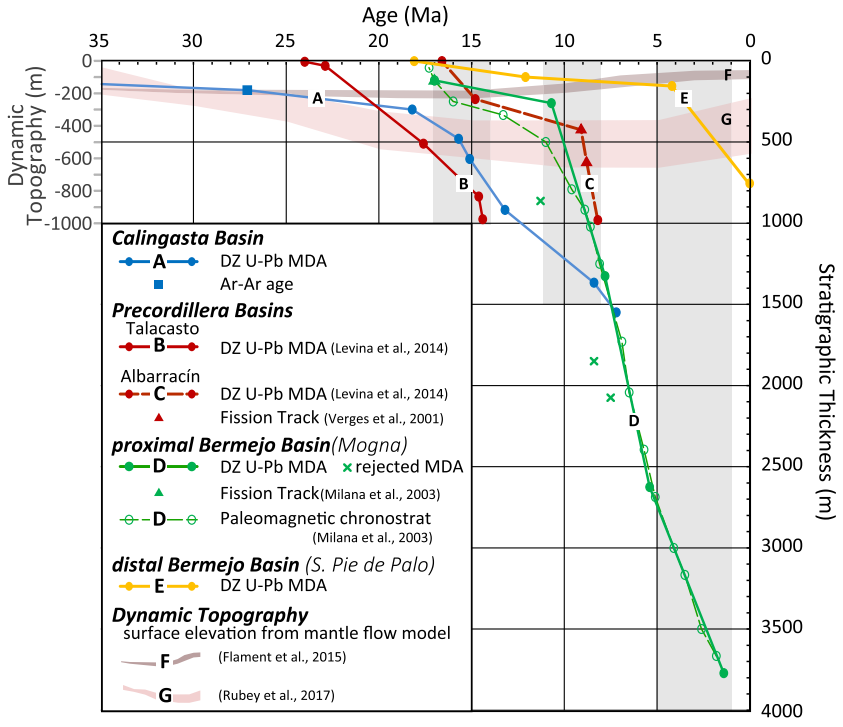

Figure 8. Cenozoic sediment accumulation history for (a) Calingasta basin (blue), (b) Precordillera basins, Talacasto section (red) and (c) Albarracín section (red dashed), (d) proximal Bermejo basin (green), and (e) distal Bermejo basin (yellow) sections. (f and g) Predicted surface elevation response to dynamic topography from mantle flow models (Flament et al., 2015; Rubey et al., 2017). With emphasis on key accumulation phases (gray boxes).

since the late Miocene. Precordillera river sands (Figure 7c; RSJN01) shows complex age distributions from mixing of Precordillera detritus with recycled Cenozoic basin fill (Capaldi et al., 2017). Modern rivers in both proximal (Figure 7d; RJAC01) and distal (Figure 7e; RPDP02) segments of the Bermejo basin show the reappearance of Andean arc and Cordilleran (0–350 Ma) age zircons, consistent with recent uplift and recycling of the proximal Cenozoic foreland basin system.

6. Sediment Accumulation History

A refined chronostratigraphic framework from new and published maximum depositional ages, dated volcanic horizons, and magnetostratigraphic data (Levina et al., 2014; Milana et al., 2003; Vergés et al., 2001) constrains the temporal and spatial variations in sediment accumulation across the retroarc system (Figure 8a). The stratigraphic age and thickness data show a systematic but time-transgressive pattern of basin accommodation from proximal (western) to distal (eastern) segments. Each basin locality recorded a similar 10–30 Myr history in which an early phase of slow accumulation (<300 m) was followed by rapid accumulation (600–3,500 m). The onset of basin accumulation was time transgressive, with initial Paleogene (>23 Ma) deposition restricted to proximal western zones followed by Neogene deposition across the basins system. Similarly, the shift from slow to rapid accumulation was also time transgressive. Rapid accumulation commenced in the proximal foreland (Calingasta, Talacasto) at 17–14 Ma (124–145 m/Myr) (Figures 8a and 8b), in medial segments (Albarracín, western Bermejo) at 11–8 Ma (367–617 m/Myr) (Figures 8c and 8d), and in distal segments (eastern Bermejo, Sierras Pampeanas) at 5 Ma (149 m/Myr) (Figure 8e).

The observed eastward progression of (a) the onset of basin accommodation and (b) the shift to rapid large-magnitude accommodation is in accordance with conceptual models and ancient examples of the cratonward advance of flexural subsidence in a foreland basin system (Decelles & Giles, 1996; Horton et al., 2001). In addition to flexural loading driven by horizontal shortening and crustal thickening, Cordilleran orogenic systems are also influenced by dynamic loading linked to mantle flow and viscous coupling

between the subducting and overriding plates (Cardozo & Jordan, 2001; Dávila & Lithgow-Bertelloni, 2013; Painter & Carrapa, 2013; Pysklywec & Mitrovica, 1999). Recent models predict temporal and spatial variations in retroarc dynamic subsidence during changes in subduction geometry (e.g., Flament et al., 2015; Rubey et al., 2017). Although dynamic subsidence may explain up to several hundred meters of subsidence, we interpret the observed large-magnitude subsidence and systematic progression of basin initiation and maximum subsidence to be best explained by flexural subsidence during the advance of crustal shortening. Nevertheless, we speculate that the relatively subdued rates of rapid accumulation in the distal foreland may be the product of localized flexural subsidence adjacent to Sierras Pampeanas basement uplifts superimposed on regional dynamic uplift driven by flat slab subduction.

7. Regional Stratigraphic and Magmatic Profiles

To delineate the Cenozoic stratigraphic and magmatic histories at 31.5°S, we present two regional east-west profiles (Figure 9). A stratigraphic profile spanning the retroarc basin system (Figure 9a) summarizes spatial and temporal stratigraphic relationships on the basis of information recorded within the five measured stratigraphic sections (Figure 3). Although there are few regionally extensive marker horizons, the new age control provided by detrital and volcanic materials (Calingasta section) enables approximate correlation of most the major stratigraphic intervals. The major clastic facies assemblages range from coarse-grained deposits of proximal alluvial fan and fluvial systems to distal fine-grained deposits of fluvial overbank and playa lake systems. Volcanic flows and relatively coarse-grained volcaniclastic facies are mostly restricted to western localities, and sandy eolian facies are limited to medial basin localities. Stratigraphic variations among the five sections consistently show a spatial transition from coarser facies in the west to finer facies in the east.

Individual measured sections show an upsection increase in grain size that generally reflects a transition from fine-grained lacustrine and distal fluvial deposits to coarse-grained fluvial to alluvial fan sandstones and conglomerates. The transition to coarser facies occurs within lower Miocene deposits in the west (Calingasta basin), middle to late Miocene deposits within Precordillera localities (Talacasto and Albarracín valleys), and latest Miocene to Pliocene deposits farther east (Bermejo basin). Collectively, these spatial contrasts in upward coarsening patterns reveal an east-west stratigraphic architecture (Figure 9a) consistent with long-term progradation of coarse-grained depositional systems from proximal western to distal eastern segments of the foreland basin system.

Eastward onlap of 24–17 Ma deposits onto pre-Cenozoic basement in the Bermejo basin is consistent with a possible forebulge unconformity, with subsequent burial by 17 to 11 Ma strata during overfilling or expansion of the basin and resulting onlap of the craton. The increase of the sediment accumulation rates from 20 to >500 m/Myr in proximal Bermejo basin at the 11 Ma transition suggest enhanced orogenic loading from the propagation of Precordillera thrusting. Hinterland derived sediment bypassed the Calingasta hinterland basin and Precordillera wedge-top depocenters, and ultimately deposited in the Bermejo foredeep deposystem. Late Miocene Bermejo basin deposits consist of an upward coarsening thick fluvial megafan sequence associated with enhanced shortening and crustal loading in the orogen, rapid erosion and sediment transport, and increased sediment supply to the foreland basin.

To assess time-space patterns of arc magmatism, we compiled detrital zircon age distributions (Capaldi et al., 2017; Levina et al., 2014; this study) and igneous bedrock ages (Pilger, 2018) along a regional arc-perpendicular profile between 29 to 33°S (Figure 9b). Bedrock data were plotted relative to present-day longitude and filtered to remove duplicates of K-Ar, $^{40}Ar/^{39}Ar$, and zircon U-Pb ages. Additionally, the distribution of igneous rocks was not palinspastically adjusted to restore Andean shortening, plotted data represent minimum widths of the Andean arc. The igneous bedrock distribution profile reveals several shifts in arc magmatism: (1) Initial arc magmatism at 35 to 25 Ma is focused over a narrow ~100 km zone at 70–71°W. Although the reduced number of data points may reflect diminished magmatism, we expect that it reflects the fact that these older igneous materials are largely covered by younger volcanic materials. (2) A broad ~200 km zone of magmatism was concentrated at 69–71°W from 25 to 10 Ma, with an intensified magmatism flare-up that peaked from 18 to 16 Ma and began to wane by 15 Ma. (3) A very broad region of magmatism commenced between 11 to 7 Ma across a wide swath (65–70.5°W), indicating a rapid ~400 + km inboard advance of magmatism. In addition, at ~5 Ma, a notable cessation of arc magmatism is recorded at 70–71°W, a region that had formerly served as the locus of Neogene magmatism.

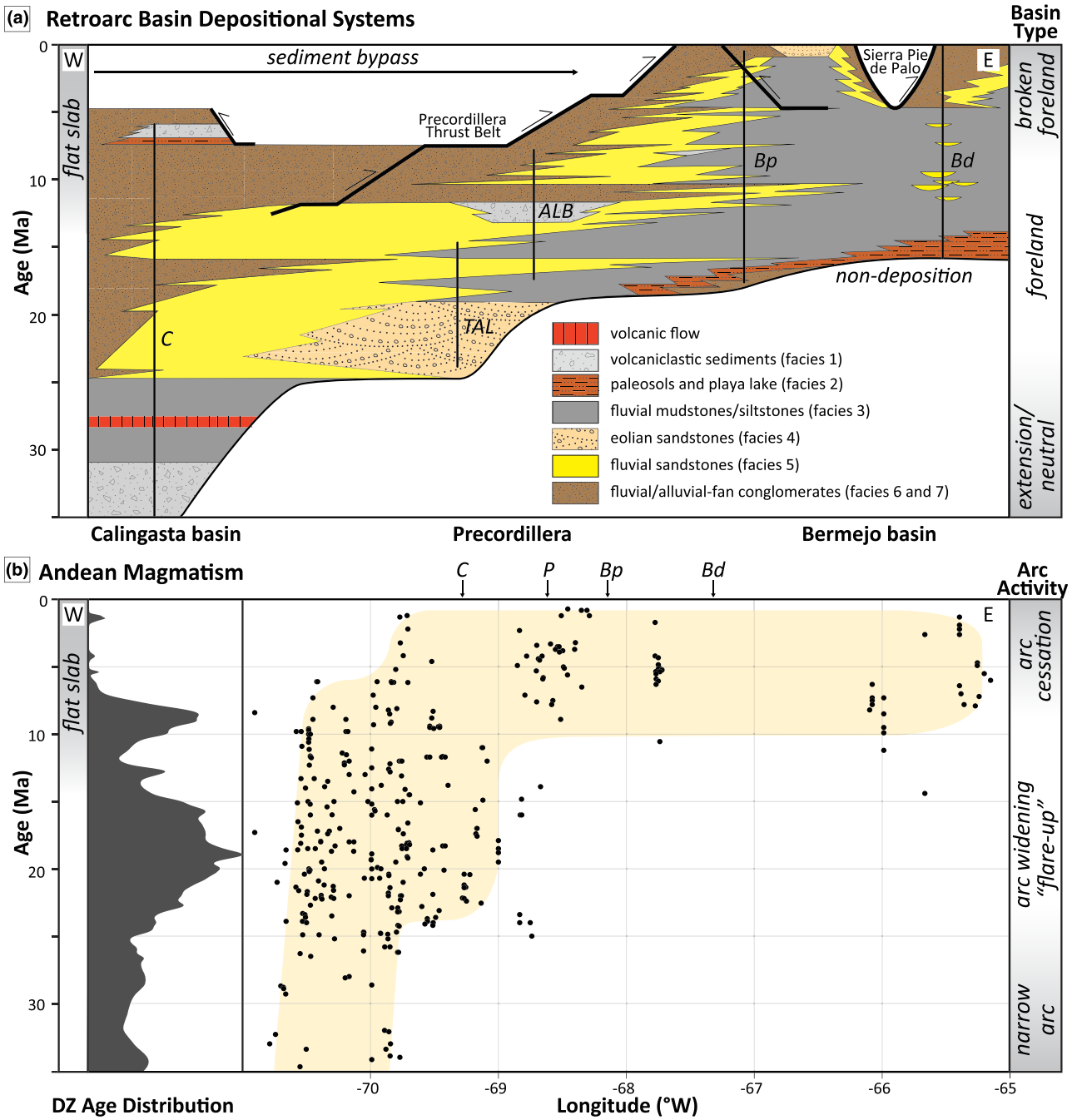

Figure 9. Spatial and temporal variation in retroarc basin deposition and Andean arc magmatism during Pampean flat-slab subduction. (a) Stratigraphic correlation plot across the Argentina retroarc basin system. Vertical black lines represent measured section locations, and Precordillera fold-thrust belt shortening patterns from (Allmendinger & Judge, 2014). (b) Cenozoic magmatic history recorded by compiled detrital zircon U-Pb age distribution depicted as probability density plot (black), and Arc volcanism migration patterns (orange) tracked by bedrock radiometric dates between 28–33°S (Pilger, 2018; black circles). Calingasta basin (C), Precordillera basins (P), Talacasto (TAL), Albarracín (ALB), proximal Bermejo basin (pB), and distal Bermejo basin (dB).

8. Discussion

Stratigraphic (Figure 3), lithofacies (Figure 4), provenance (Figures 5–7), and accumulation histories (Figure 8) establish a framework to track Cenozoic erosion, sediment transport, and basin evolution (Figure 9a). Detrital zircon age distributions and bedrock igneous ages (Pilger, 2018) provide new constraints on Andean arc magmatism and the locus of dehydration melting above the leading inboard hinge of the

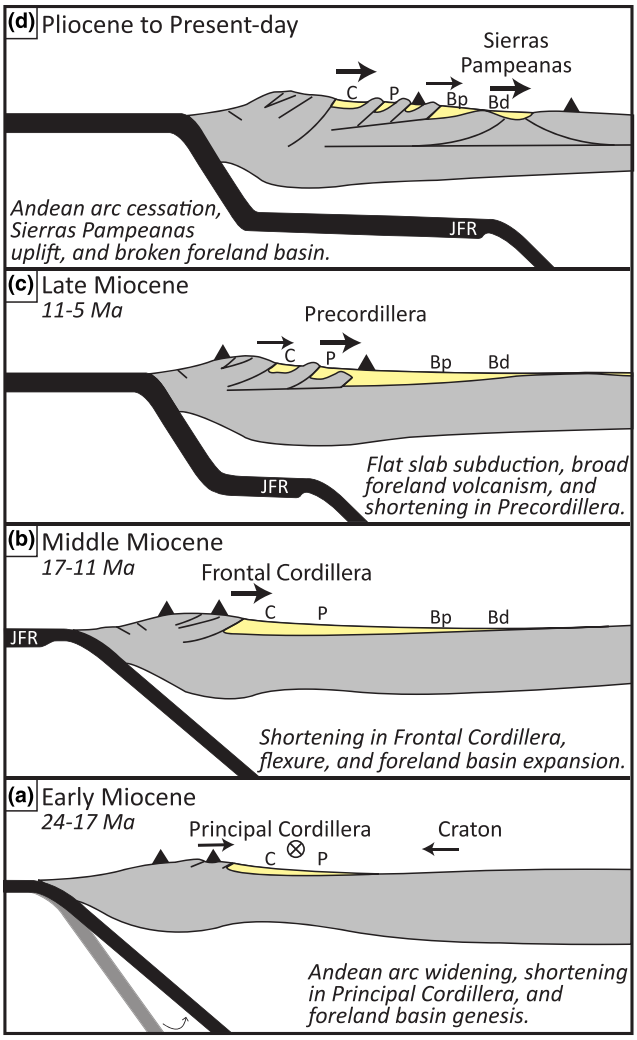

Figure 10. Argentina retroarc basin evolution in response to changing subduction regime: (a) Early Miocene; (b) Middle Miocene; (c) Late Miocene; and (d) Pliocene to the present. Includes basin deposition (yellow), sediment provenance sources (Principal Cordillera, Frontal Cordillera, Precordillera, Sierras Pampeanas, and craton), paleoflow direction (black arrow), arc magmatism front (black triangle), and location of Calingasta basin (C), Precordillera basins (P), proximal Bermejo basin (Bp), distal Bermejo basin (Bd), and Juan Fernandez Ridge (JFR).

subducted slab (Figure 9b). Integrated records of Andean igneous activity and retroarc basin evolution (in terms of sediment accumulation, sediment routing, and basin configuration, Table S6) provide insights into the relationships among subduction, magmatism, erosion, and subsidence during four key time frames (Figure 10): (1) early Miocene (24–17 Ma); (2) middle Miocene (17–11 Ma); (3) late Miocene (11–5 Ma); and (4) Pliocene to present (5–0 Ma).

8.1. Early Miocene Incipient Foreland Basin

Early foreland basin subsidence is synchronous with an increase in magmatic activity and broadening of the Andean magmatic arc (~200 km), which reflects an initial decrease in subduction angle (Figure 10a). During this time regional paleodrainage patterns changed from predominately eolian deposition and N axial transport, to an extensive east flowing braided river depositional system. Fluvial deposits in the proximal and medial basin localities were eroded from Principal Cordilleran sources, in contrast to distal localities that preserve gravely facies (Rio Salado Formation) from the eastern craton (Figure 9a). Flexural response to early orogenic loading in the Principal Cordillera may also have included a broad, low-amplitude forebulge uplift in the distal cratonic region, with contrasting western orogenic and eastern cratonic sediment sources (Figure 10a; Horton, 2018b; Mackaman-Lofland et al., 2019, 2020; Pinto et al., 2018). Principal Cordilleran deformation may be linked to a plate tectonic transition to enhanced trench-perpendicular convergence, and initial oblique subduction of the Juan Fernandez Ridge along the South American margin (Figure 10a; Martinod et al., 2010; Yáñez et al., 2001).

8.2. Middle Miocene Foreland Basin Expansion

The middle Miocene phase development of an extensive foreland basin is associated with continued magmatism and crustal thickening driven by shortening in the Frontal Cordillera (Figure 10b). Contrasting sediment accumulation records across the regional transect (Figures 8 and 9) suggest a regional basin architecture involving a foredeep in the west (Calingasta and Precordillera segments) and distal foredeep to forebulge in the east (Bermejo basin). Eastward advance of coarse-grained depo systems across the foreland basin system corresponded unroofing of initial Andean arc rocks and subsequent erosion into Frontal Cordillera igneous basement. Early Miocene thermochronometric cooling ages attest to shortening-related exhumation in the Frontal Cordillera (Hoke, Graber, et al., 2014; Lossada et al., 2017; Riesner et al., 2019). Erosion of the Frontal Cordilleran further expressed in middle-Miocene deposits to the southwest (Manantiales basin; Mackaman-Lofland et al., 2020: Pinto et al., 2018), southeast (Cachueta basin: Buelow et al., 2018), northern Bermejo basin (Fosdick et al., 2015; Jordan et al., 1996), and northeastern Bermejo basin (Ischigualasto-Villa Unión basin: Lemos-Santos et al., 2019). Igneous geochemical signatures suggest increased crustal contributions related to continued crustal thickening (>50 km) (Litvak et al., 2018; Jones et al., 2015; Kay et al., 1991). Diminished arc activity from 15 to 12 Ma overlaps with a reported shift to enhanced strike-slip conditions in the Andean hinterland at 30°S (Giambiagi et al., 2017), possibly linked to increased gravitational potential energy in thickened orogenic crust (DeCelles et al., 2015).

8.3. Late Miocene Flat-Slab Subduction

Arrival and subduction of the Juan Fernandez Ridge is documented by pronounced eastward advance of volcanism, shortening in the Precordillera thrust belt, and rapid subsidence in the Bermejo basin (Figure 10c). Increased late Miocene volcanic activity was synchronous with an inboard magmatic

sweep (>450 km) toward the craton (Figure 9b), characteristic of subduction flattening (Haschke et al., 2006; Ramos & Folguera, 2009). Nazca plate reconstructions indicate a late Miocene (~11 Ma) arrival of the Juan Fernandez Ridge to the Chile trench at 31°S (Yáñez et al., 2001). Subduction of the relatively thick, younger oceanic crust of the Juan Fernandez Ridge has long been cited as a potential driver of Pampean flat slab subduction (Kay et al., 1991; Pilger, 1981; Porter et al., 2012; Ranero et al., 2006; Yáñez et al., 2001). Sediment provenance records require late Miocene erosion of Precordillera and recycled foreland basin sources (Buelow et al., 2018; Fosdick et al., 2015; Levina et al., 2014; Vergés et al., 2001). Western basin localities (Calingasta and Precordillera) show a decrease in sediment accumulation coeval with alluvial fan deposition and proximal sediment sources. These changes are consistent with wedge-top deposition in the west as the foredeep depocenter migrated eastward toward the Bermejo basin (Beer et al., 1990; Levina et al., 2014; Suriano et al., 2017; Vergés et al., 2001). At 8 Ma, the Calingasta basin records facies change from alluvial fan to fluvially reworked volcaniclastics and interbedded lacustrine depositional environments suggestive of an internally drained hinterland basin system (Hoke, Giambiagi, et al., 2014; Ruskin & Jordan, 2007; Val et al., 2016). Changes in depositional environment, sediment provenance, and advance of flexural subsidence into the Bermejo foreland basin indicate shortening along the Precordillera fold-thrust belt initiated by 12–10 Ma at 31°S, consistent with previous estimates (Allmendinger & Judge, 2014; Cristallini & Ramos, 2000; Fosdick et al., 2015; Jordan et al., 1996; Walcek & Hoke, 2012).

8.4. Pliocene-Quaternary Broken Foreland Basin

Contrasting records of subsidence and sediment dispersal reveal a shift from a once continuous flexural foreland basin to a series of broken foreland depocenters driven by Sierras Pampeanas province (Figure 10d; Jordan, 1995). The distal Bermejo basin recorded uplift of the Sierra Pie de Palo to 5 Ma, consistent with sedimentary and thermochronometric records along strike to the north (Carrapa et al., 2008; Coughlin et al., 1998; Löbens et al., 2013; Ortiz et al., 2015; Stevens-Goddard & Carrapa, 2017). Major igneous activity within the Andean magmatic arc shut off by ~5 Ma, with diffuse eastern volcanic centers continuing until ~2 Ma (Figure 9b; Kay & Abbruzzi, 1996). Flat slab subduction may bulldoze lower continental mantle lithosphere into the asthenosphere wedge, terminating dehydration melting and associated magmatism (Axen et al., 2018; Bishop et al., 2017). Seismic tomographic and receiver function results indicate limited mantle wedge material between thickened (~60–70 km) South American crust and ~300 km long subhorizontal segment of the subducted Nazca plate at 100 km depth (Wagner et al., 2005, 2006; Ammirati et al., 2016; Porter et al., 2012; Ward et al., 2013). The significant redistribution of mass at depth may exert pulse of dynamic subsidence or uplift (Dávila & Lithgow-Bertelloni, 2015; Flament et al., 2015; Rubey et al., 2017). We propose that transient dynamic subsidence at the leading hinge between flat and normal slab segments may help explain the enhanced thickness (~4 km) of upper Miocene to Pleistocene deposits in the Bermejo foreland basin (Figures 9b and 10c).

9. Conclusions

1. The Neogene response to flat slab subduction in the southern Central Andes involved foreland progression of coarse grained deposystems, a shift in deformation from a thin-skinned thrust belt to a series of basement involved foreland uplifts, eastward migration of zones of rapid accommodation within the retroarc basin system, and a systematic inboard sweep in arc volcanism.
2. Measured stratigraphic sections integrated with zircon U-Pb and 40Ar/39Ar ages facilitated new basin-scale correlations across a regional Andean transect in Argentina at 32.5°S. Individual basin localities show an upsection increase in grain size that generally reflects a transition from fine-grained lacustrine and distal fluvial deposits to coarse-grained fluvial to alluvial fan sandstones and conglomerates. Stratigraphic correlations reveal long-term (10–30 Myr) advance of coarse-grained depositional systems from proximal western (Calingasta basin), to central (Talacasto and Albarracín basins), to eastern (Bermejo foreland basin) segments of the retroarc basin system.
3. Sediment provenance constraints from detrital zircon U-Pb ages and conglomerate clast compositions record sequential unroofing of the Principal Cordillera (24–17 Ma), Frontal Cordillera (17–11 Ma), Precordillera (11–5 Ma), and Sierras Pampeanas (5–0 Ma). Middle Miocene initiation of flat slab subduction was marked at 12–10 Ma by significant changes in depocenter position, and sediment sources as focused erosion migrated toward the foreland.

4. Stratigraphic age and thickness data show a systematic and time-transgressive onset of basin accumulation with initial Paleogene (>24 Ma) deposition restricted to proximal western zones followed by Neogene deposition across the eastern basin system. The observed eastward progression of both the onset of basin accommodation and the shift to rapid large-magnitude accommodation—in the proximal foreland (Calingasta, Talacasto) at 17–14 Ma and in medial segments (Albarracín, proximal Bermejo) at 11–8 Ma—is in accordance with the cratonward advance of flexural subsidence in a foreland basin system. Rapid accumulation in distal segments (eastern Bermejo, Sierras Pampeanas) at 5 Ma marks the shift from a once continuous flexural foreland basin (24 to 5 Ma) to a series of broken foreland depocenters driven by Sierras Pampeanas uplift in response to flat slab subduction.
5. Regional igneous bedrock and detrital U-Pb age patterns define Neogene broadening of the Andean magmatic arc associated with changes in the geometry of the subducted slab. The Miocene Andean arc transitioned to an ~200 km broad magmatic zone with an intensified igneous activity that peaked from 18 to 16 Ma, likely driven by initial shallowing of subduction. Increased magmatic activity at 11–8 Ma was synchronous with an inboard (>450 km) sweep of magmatism toward the craton, characteristic of subduction flattening. By ~5 Ma, arc magmatism ceased in the Andean region that had formerly served as the locus of Neogene magmatism.

Data Availability Statement

Readers can access new Ar-Ar and zircon U-Pb data by name, sample location, and analyses type at geochron.org (https://www.geochron.org/results.php?pkey=29370) and in the supporting information (Data Sets S1–S6). Site licensed under Creative Commons Attribution-Noncommercial-Share Alike 3.0 and part of the IEDA Data Facility.

Acknowledgments

This research was supported by a National Science Foundation (NSF) grant (EAR-1348031) awarded to B. K. Horton and N. R. McKenzie, and research grants from GSA, AAPG, SEPM, and the Jackson School of Geosciences awarded to T. N. Capaldi. We thank Margo Odlum, Mark Helper, Peter Flaig, Ron Steel, Ryan Anderson, Sarah George, Kristina Butler, Lily Jackson, Kelly Thomson, Greg Hoke, Facundo Fuentes, Matt Heizler, and Lisa Stockli for helpful discussions. Constructive comments from Peter DeCelles and an anonymous reviewer significantly improved the manuscript.

References

Allmendinger, R. W., & Judge, P. A. (2014). The argentine Precordillera: A foreland thrust belt proximal to the subducted plate. *Geosphere*, *10*, 1203–1218. https://doi.org/10.1130/ges01062.1

Alvarado, P., Pardo, M., Gilbert, H., Miranda, S., Anderson, M., Saez, M., & Beck, S. (2009). Flat-slab subduction and crustal models for the seismically active Sierras Pampeanas region of Argentina. In S. M. Kay, V. A. Ramos, & W. R. Dickinson (Eds.), *Backbone of the Americas: Shallow subduction, plateau uplift, and ridge and terrane collision* (Vol. 204, pp. 261–278). CO, USA: Geological Society of America Memoir. https://doi.org/10.1130/2009.1204(12)

Amidon, W. H., Burbank, D. W., & Gehrels, G. E. (2005). Construction of detrital mineral populations: Insights from mixing of U-Pb zircon ages in Himalayan rivers. *Basin Research*, *17*(4), 463–485. https://doi.org/10.1111/j.1365-2117.2005.00279.x

Ammirati, J. B., Pérez Luján, S., Alvarado, P., Beck, S., Rocher, S., & Zandt, G. (2016). High-resolution images above the Pampean flat slab of Argentina (31–32°S) from local receiver functions: Implications on regional tectonics. *Earth and Planetary Science Letters*, *450*, 29–39. https://doi.org/10.1016/j.epsl.2016.06.018

Axen, G. J., van Wijk, J. W., & Currie, C. A. (2018). Basal continental mantle lithosphere displaced by flat-slab subduction. *Nature Geoscience*, *11*(12), 961. https://doi.org/10.1038/s41561-018-0263-9

Bahlburg, H., Vervoort, J. D., Du Frane, S. A., Bock, B., Augustsson, C., & Reimann, C. (2009). Timing of crust formation and recycling in accretionary orogens: Insights learned from the western margin of South America. *Earth-Science Reviews*, *97*(1–4), 215–241. https://doi.org/10.1016/j.earscirev.2009.10.006

Barazangi, M., & Isacks, B. L. (1976). Spatial distribution of earthquakes and subduction of the Nazca plate beneath South America. *Geology*, *4*(11), 686–692. https://doi.org/10.1130/0091-7613(1976)4<686:SDOEAS>2.0.CO;2

Beer, J. A., Allmendinger, R. W., Figueroa, D. E., & Jordan, T. E. (1990). Seismic stratigraphy of a Neogene piggyback basin, Argentina. *American Association of Petroleum Geologists Bulletin*, *74*, 1183–1202. https://doi.org/10.1306/0c9b244d-1710-11d7-8645000102c1865d

Bellahsen, N., Sébrier, M., & Siame, L. (2016). Crustal shortening at the sierra pie de Palo (sierras Pampeanas, Argentina): Near-surface basement folding and thrusting. *Geological Magazine*, *153*(5–6), 992–1012. https://doi.org/10.1017/S0016756816000467

Bird, P. (1984). Formation of the Rocky Mountains foreland and Great Plains. *Tectonics*, *3*(7), 741–758. https://doi.org/10.1029/TC003i007p00741

Bishop, B. T., Beck, S. L., Zandt, G., Wagner, L., Long, M., Knezevic Antonijevic, S., et al. (2017). Causes and consequences of flat-slab subduction in southern Peru. *Geosphere*, *13*(5), 1392–1407. https://doi.org/10.1130/GES01440.1

Buelow, E. K., Suriano, J., Mahoney, J. B., Kimbrough, D. L., Mescua, J. F., Giambiagi, L. B., & Hoke, G. D. (2018). Sedimentologic and stratigraphic evolution of the Cacheuta basin: Constraints on the development of the Miocene retroarc foreland basin, south-Central Andes. *Lithosphere*, *10*(3), 366–391. https://doi.org/10.1130/L709.1

Burns, C. E., Mountney, N. P., Hodgson, D. M., & Colombera, L. (2017). Anatomy and dimensions of fluvial crevasse-splay deposits: Examples from the Cretaceous Castlegate Sandstone and Neslen Formation, Utah, U.S.A. *Sedimentary Geology*, *351*, 21–35. https://doi.org/10.1016/j.sedgeo.2017.02.003

Cahill, T., & Isacks, B. L. (1992). Seismicity and shape of the subducted Nazca plate. *Journal of Geophysical Research*, *97*(B12), 17,503–17,529. https://doi.org/10.1029/92JB00493

Capaldi, T. N., George, S. W. M., Hirtz, J. A., Horton, B. K., & Stockli, D. F. (2019). Fluvial and Eolian sediment mixing during changing climate conditions recorded in Holocene Andean foreland deposits from Argentina (31–33°S). *Frontiers in Earth Science*, *7*. https://doi.org/10.3389/feart.2019.00298

Capaldi, T. N., Horton, B. K., McKenzie, N. R., Stockli, D. F., & Odlum, M. L. (2017). Sediment provenance in contractional orogens: The detrital zircon record from modern rivers in the Andean fold-thrust belt and foreland basin of western Argentina. *Earth and Planetary Science Letters*, *479*, 83–97. https://doi.org/10.1016/j.epsl.2017.09.001

Capezzuoli, E., Gandin, A., & Pedley, M. (2014). Decoding tufa and travertine (fresh water carbonates) in the sedimentary record: The state of the art. *Sedimentology*, *61*(1), 1–21. https://doi.org/10.1111/sed.12075

Cardozo, N., & Jordan, T. (2001). Causes of spatially variable tectonic subsidence in the Miocene Bermejo foreland basin, Argentina. *Basin Research*, *13*(3), 335–357. https://doi.org/10.1046/j.0950-091x.2001.00154.x

Carrapa, B., Hauer, J., Schoenbohm, L., Strecker, M. R., Schmitt, A. K., Villanueva, A., & Sosa Gomez, J. (2008). Dynamics of deformation and sedimentation in the northern sierras Pampeanas: An integrated study of the Neogene Fiambalá basin, NW Argentina. *Geological Society of America Bulletin*, *120*(11–12), 1518–1543. https://doi.org/10.1130/B26111.1

Charrier, R., Ramos, V. A., Tapia, F., & Sagripanti, L. (2015). Tectono-stratigraphic evolution of the Andean Orogen between 31 and 37 S (Chile and Western Argentina). *Geological Society, London, Special Publications*, *399*(1), 13–61. https://doi.org/10.1144/SP399.20

Chew, D. M., Schaltegger, U., Košler, J., Whitehouse, M. J., Gutjahr, M., Spikings, R. A., & Mišković, A. (2007). U-Pb geochronologic evidence for the evolution of the Gondwanan margin of the north-Central Andes. *Bulletin of the Geological Society of America*, *119*(5-6), 697–711. https://doi.org/10.1130/B26080.1

Coira, B. L., Davidson, J. D., Mpodozis, C., & Ramos, V. A. (1982). Tectonic and magmatic evolution of the Andes of northern Argentina and Chile. *Earth Science Reviews*, *18*(3-4), 303–332. https://doi.org/10.1016/0012-8252(82)90042-3

Cole, R. B., & Decelles, P. G. (1991). Subaerial to submarine transitions in early Miocene pyroclastic flow deposits, southern San Joaquin basin, California. *Geological Society of America Bulletin*, *103*, 221–235. https://doi.org/10.1130/0016-7606(1991)103<0221:ststie>2.3.co;2

Coney, P. J. (1978). Mesozoic-Cenozoic Cordilleran plate tectonics. In R. B. Smith, & G. P. Eaton (Eds.), *Cenozoic tectonics and regional geophysics of the western Cordillera* (Vol. 152, pp. 33–50). CO, USA: Geological Society of America Memoir. https://doi.org/10.1130/MEM152-p33

Coney, P. J., & Reynolds, S. J. (1977). Cordilleran benioff zones. *Nature*, *270*(5636), 403.

Constenius, K. N. (1996). Late Paleogene extensional collapse of the cordilleran foreland fold and thrust belt. *Geological Society of America Bulletin*, *108*(1), 20–39. https://doi.org/10.1130/0016-7606(1996)108<0020:LPECOT>2.3.CO;2

Constenius, K. N., Esser, R. P., & Layer, P. W. (2003). Extensional collapse of the Charleston-Nebo salient and its relationship to space-time variations in Cor-Dilleran Orogenic Belt Tectonism and continental stratigraphy. In *Cenozoic systems of the western United States* (pp. 303–353). CO, USA: Society of Economic Paleontologists and Mineralogists.

Coughlin, T. J., O'Sullivan, P. B., Kohn, B. P., & Holcombe, R. J. (1998). Apatite fission-track thermochronology of the sierras Pampeanas, central western Argentina: Implications for the mechanism of plateau uplift in the Andes. *Geology*, *26*(11), 999–1002. https://doi.org/10.1130/0091-7613(1998)026<0999:AFTTOT>2.3.CO;2

Coutts, D. S., Matthews, W. A., & Hubbard, S. M. (2019). Assessment of widely used methods to derive depositional ages from detrital zircon populations. *Geoscience Frontiers*, *10*(4), 1421–1435. https://doi.org/10.1016/j.gsf.2018.11.002

Cristallini, E. O., & Ramos, V. A. (2000). Thick-skinned and thin-skinned thrusting in the La Ramada fold and thrust belt: Crustal evolution of the high Andes of San Juan, Argentina (32°SL). *Tectonophysics*, *317*(3–4), 205–235. https://doi.org/10.1016/S0040-1951(99)00276-0

Cross, T. A., & Pilger, R. H. (1982). Controls of subduction geometry location of magmatic arcs and tectonics of arc and back-arc regions. *Geological Society of America Bulletin*, *93*, 545–562. https://doi.org/10.1130/0016-7606(1982)93<545:cosglo>2.0.co;2

Cuerda, A., Varela, R., & Iniguez, A. M. (1983). Secuencia salifera en el terciario de Nikisanga, Sierra Pie de Palo, Provincia de San Juan. *Asociacion Geologica Argentina*, *38*, 412–420.

Damanti, J. F. (1993). Geomorphic and structural controls on facies patterns and sediment composition in a modern foreland basin. In M. Marzo, & C. Puigdefábregas (Eds.), *Alluvial sedimentation* (Vol. 17, pp. 221–233). Belgium: International Association Sedimentologists Special Publication.

Dávila, F. M., & Lithgow-Bertelloni, C. (2013). Dynamic topography in South America. *Journal of South American Earth Sciences*, *43*, 127–144. https://doi.org/10.1016/j.jsames.2012.12.002

Dávila, F. M., & Lithgow-Bertelloni, C. (2015). Dynamic uplift during slab flattening. *Earth and Planetary Science Letters*, *425*, 34–43. https://doi.org/10.1016/j.epsl.2015.05.026

Dávila, F. M., Lithgow-Bertelloni, C., & Giménez, M. (2010). Tectonic and dynamic controls on the topography and subsidence of the argentine pampas: The role of the flat slab. *Earth and Planetary Science Letters*, *295*(1–2), 187–194. https://doi.org/10.1016/j.epsl.2010.03.039

DeCelles, P. G., Carrapa, B., Horton, B. K., McNabb, J., Gehrels, G. E., & Boyd, J. (2015). The Miocene Arizaro Basin, central Andean hinterland: Response to partial lithosphere removal? In P. G. DeCelles, M. N. Ducea, B. Carrapa, & P. A. Kapp (Eds.), *Geodynamics of a Cordilleran Orogenic System: The Central Andes of Argentina and Northern Chile* (Vol. 212, pp. 359–386). CO, USA: Geological Society of America Memoirs. https://doi.org/10.1130/2015.1212(18)

DeCelles, P. G., & Cavazza, W. (1999). A comparison of fluvial megafans in the cordilleran (upper cretaceous) and modern Himalayan foreland basin systems. *Bulletin of the Geological Society of America*, *111*(9), 1315–1334. https://doi.org/10.1130/0016-7606(1999)111<1315:ACOFMI>2.3.CO;2

Decelles, P. G., & Giles, K. A. (1996). Foreland Basin systems Foreland basin systems. *Basin Research*, *8*(2), 105–123. https://doi.org/10.1046/j.1365-2117.1996.01491.x

DeCelles, P. G., Zandt, G., Beck, S. L., Currie, C. A., Ducea, M. N., Kapp, P., et al. (2015). Cyclical orogenic processes in the Cenozoic Central Andes. In P. G. DeCelles, M. N. Ducea, B. Carrapa, & P. A. Kapp (Eds.), *Geodynamics of a cordilleran Orogenic system: The Central Andes of Argentina and northern Chile* (Vol. 212, pp. 459–490). CO, USA: Geological Society of America Memoirs. https://doi.org/10.1130/9780813712123

Del Rey, A., Deckart, K., Arriagada, C., & Martínez, F. (2016). Resolving the paradigm of the late Paleozoic–Triassic Chilean magmatism: Isotopic approach. *Gondwana Research*, *37*, 172–181. https://doi.org/10.1016/j.gr.2016.06.008

Dickinson, W. R., & Gehrels, G. E. (2009). Use of U–Pb ages of detrital zircons to infer maximum depositional ages of strata: A test against a Colorado plateau Mesozoic database. *Earth and Planetary Science Letters*, *288*(1–2), 115–125. https://doi.org/10.1016/j.epsl.2009.09.013

Dickinson, W. R., Klute, M. A., Hayes, M. J., Janecke, S. U., Lundin, E. R., McKittrick, M. A., & Olivares, M. D. (1988). Paleogeographic and paletotectonic setting of Laramide sedimentary basins in the central Rocky-Mountain region. *Geological Society of America Bulletin*, *100*(7), 1023–1039. https://doi.org/10.1130/0016-7606(1988)100<1023:papsol>2.3.co;2

Dickinson, W. R., & Snyder, W. S. (1978). Plate tectonics of the Laramide orogeny. In V. M. Ed (Ed.), *Laramide folding associated with basement block faulting in the western United States* (Vol. 151, pp. 355–366). CO, USA: Geological Society of America Memoir. https://doi.org/10.1130/MEM151-p355

Ducea, M. N., Giosan, L., Carter, A., Balica, C., Stoica, A. M., Roban, R. D., et al. (2018). U-PB detrital zircon geochronology of the lower Danube and its tributaries: Implications for the Geology of the Carpathians. *Geochemistry, Geophysics, Geosystems*, *19*, 3208–3223. https://doi.org/10.1029/2018GC007659

Ducea, M. N., Otamendi, J. E., Bergantz, G., Stair, K. M., Valencia, V. A., & Gehrels, G. (2010). Timing constraints on building an intermediate plutonic arc crustal section: U-Pb zircon geochronology of the sierra Valle Fertil-La Huerta, Famatinian arc, Argentina. *Tectonics*, *29*, TC4002. https://doi.org/10.1029/2009TC002615

Erslev, E. A. (1993). Thrusts, backthrusts and detachment of Laramide foreland arches. In C. J. Schmidt, R. Chase, & E. A. Erslev (Eds.), *Laramide basement deformation in the Rocky Mountain foreland of the western United States* (Vol. 280, pp. 125–146). CO, USA: Geological Society of America Special Paper.

Erslev, E. A. (2005). *2D Laramide geometries and kinematics of the Rocky Mountains, western USA*, (Vol. 154, pp. 7–20). Washington DC: American Geophysical Union Geophysical Monograph Series.

Fan, M., & Carrapa, B. (2014). Late cretaceous–early Eocene Laramide uplift, exhumation, and basin subsidence in Wyoming: Crustal responses to flat slab subduction. *Tectonics*, *33*, 509–529. https://doi.org/10.1002/2012TC003221

Finzel, E. S. (2019). Partitioning pervasive detrital Geochronologic age distributions in the southern Alaskan Forearc. *Frontiers in Earth Science*, *7*, 1–17. https://doi.org/10.3389/feart.2019.00217

Finzel, E. S., Trop, J. M., Ridgway, K. D., & Enkelmann, E. (2011). Upper plate proxies for flat-slab subduction processes in southern Alaska. *Earth and Planetary Science Letters*, *303*(3–4), 348–360. https://doi.org/10.1016/j.epsl.2011.01.014

Flament, N., Gurnis, M., Müller, R. D., Bower, D. J., & Husson, L. (2015). Influence of subduction history on south American topography. *Earth and Planetary Science Letters*, *430*, 9–18. https://doi.org/10.1016/j.epsl.2015.08.006

Fosdick, J. C., Carrapa, B., & Ortíz, G. (2015). Faulting and erosion in the argentine Precordillera during changes in subduction regime: Reconciling bedrock cooling and detrital records. *Earth and Planetary Science Letters*, *432*, 73–83. https://doi.org/10.1016/j.epsl.2015.09.041

Fosdick, J. C., Reat, E. J., Carrapa, B., Ortiz, G., & Alvarado, P. M. (2017). Retroarc basin reorganization and aridification during Paleogene uplift of the southern Central Andes. *Tectonics*, *36*, 493–514. https://doi.org/10.1002/2016TC004400

Giambiagi, L., Álvarez, P. P., Creixell, C., Mardonez, D., Murillo, I., Velásquez, R., et al. (2017). Cenozoic shift from compression to strike-slip stress regime in the high Andes at 30°S, during the shallowing of the slab: Implications for the El Indio/Tambo mineral district. *Tectonics*, *36*, 2714–2735. https://doi.org/10.1002/2017TC004608

González Bonorino, F. (1950). Algunos problemas geológicos de las Sierras Pampeanas. *Revista de la Asociación Geológica Argentina*, *5*(3), 81–110.

Guillaume, B., Martinod, J., & Espurt, N. (2009). Variations of slab dip and overriding plate tectonics during subduction: Insights from analogue modelling. *Tectonophysics*, *463*(1-4), 167–174. https://doi.org/10.1016/j.tecto.2008.09.043

Gurnis, M. (1992). Rapid continental subsidence following the initiation and evolution of subduction. *Science*, *255*(5051), 1556–1558. https://doi.org/10.1126/science.255.5051.1556

Gutscher, M. A., Spakman, W., Bijwaard, H., & Engdahl, E. R. (2000). Geodynamics of flat subduction: Seismicity and tomographic constraints from the Andean margin. *Tectonics*, *19*(5), 814–833. https://doi.org/10.1029/1999TC001152

Haschke, M., Günther, A., Melnick, D., Echtler, H., Reutter, K. J., Scheuber, E., & Oncken, O. (2006). Central and southern Andean tectonic evolution inferred from arc magmatism. *In The Andes*, (pp. 337–353). Berlin, Heidelberg: Springer. https://doi.org/10.1007/978-3-540-48684-8_16

Heller, P. L., & Liu, L. (2016). Dynamic topography and vertical motion of the US Rocky Mountain region prior to and during the Laramide orogeny. *GSA Bulletin*, *128*(5–6), 973–988. https://doi.org/10.1130/B31431.1

Heredia, N., Rodriguez-Fernandez, L. R., Gallastegui, G., Busquets, P., & Colombo, F. (2002). Geological setting of the Argentine Frontal Cordillera in the flat-slab segment (30°00′–31°30′S latitude). *Journal of South American Earth Sciences*, *15*, 79–99. https://doi.org/10.1016/s0895-9811(02)00007-x

Hervé, F., Fanning, C. M., Calderon, M., & Mpodozis, C. (2014). Early Permian to late Triassic batholiths of the Chilean frontal cordillera (28-31 S): SHRIMP U-Pb zircon ages and Lu-Hf and O isotope systems. *Lithos*, *184-187*, 436–446. https://doi.org/10.1016/j.lithos.2013.10.018

Hilley, G. E., Strecker, M. R., & Ramos, V. A. (2004). Growth and erosion of fold-and-thrust belts with application to the Aconcagua fold-and-thrust belt, Argentina. *Journal of Geophysical Research*, *109*, B01410. https://doi.org/10.1029/2002JB002282

Hoke, G. D., Giambiagi, L. B., Garzione, C. N., Mahoney, J. B., & Strecker, M. R. (2014). Neogene paleoelevation of intermontane basins in a narrow, compressional mountain range, southern Central Andes of Argentina. *Earth and Planetary Science Letters*, *406*, 153–164. https://doi.org/10.1016/j.epsl.2014.08.032

Hoke, G. D., Graber, N. R., Mescua, J. F., Giambiagi, L. B., Fitzgerald, P. G., & Metcalf, J. R. (2014). Near pure surface uplift of the Argentine Frontal Cordillera: Insights from (U-Th)/he thermochronometry and geomorphic analysis. *Geological Society, London, Special Publications*, *399*(1), 383–399. https://doi.org/10.1144/SP399.4

Horton, B. K. (2018a). Tectonic regimes of the central and southern Andes: Responses to variations in plate coupling during subduction. *Tectonics*, *37*, 402–429. https://doi.org/10.1002/2017TC004624

Horton, B. K. (2018b). Sedimentary record of Andean mountain building. *Earth Science Reviews*, *178*, 279–309. https://doi.org/10.1016/j.earscirev.2017.11.025

Horton, B. K., Anderson, V. J., Caballero, V., Saylor, J. E., Nie, J., Parra, M., & Mora, A. (2015). Application of detrital zircon U-Pb geochronology to surface and subsurface correlations of provenance, paleodrainage, and tectonics of the middle Magdalena Valley basin of Colombia. *Geosphere*, *11*(6), 1790–1811. https://doi.org/10.1130/GES01251.1

Horton, B. K., & DeCelles, P. G. (2001). Modern and ancient fluvial megafans in the foreland basin system of the Central Andes, southern Bolivia: Implications for drainage network evolution in foldthrust belts. *Basin Research*, *13*(1), 43–63. https://doi.org/10.1046/j.1365-2117.2001.00137.x

Horton, B. K., Fuentes, F., Boll, A., Starck, D., Ramirez, S. G., & Stockli, D. F. (2016). Andean stratigraphic record of the transition from backarc extension to orogenic shortening: A case study from the northern Neuquén Basin, Argentina. *Journal of South America Earth Sciences*, *71*, 17–40. https://doi.org/10.1016/j.jsames.2016.06.003

Horton, B. K., Hampton, B. A., & Waanders, G. L. (2001). Paleogene synorogenic sedimentation in the Altiplano plateau and implications for initial mountain building in the Central Andes. *Bulletin of the Geological Society of America*, *113*, 1387–1400. https://doi.org/10.1130/0016-7606

Horton, B. K., & Schmitt, J. G. (1996). Sedimentology of a lacustrine fan-delta system, Miocene horse camp formation, Nevada, USA. *Sedimentology*, *43*(1), 133–155. https://doi.org/10.1111/j.1365-3091.1996.tb01464.x

Humphreys, E. D. (1995). Post-Laramide removal of the Farallon slab, western United States. *Geology*, *23*(11), 987–990. https://doi.org/10.1130/0091-7613(1995)023<0987:PLROTF>2.3.CO;2

Iaffaldano, G., Bunge, H. P., & Dixon, T. H. (2006). Feedback between mountain belt growth and plate convergence. *Geology*, *34*(10), 893–896. https://doi.org/10.1130/G22661.1

Irigoyen, M. V., Buchan, K. L., & Brown, R. L. (2000). Magnetostratigraphy of Neogene Andean foreland-basin strata, lat 33°S, Mendoza Province, Argentina. *GSA Bulletin*, *112*(6), 803–816. https://doi.org/10.1130/0016-7606(2000)112<803:MONAFS>2.0.CO;2

Jackson, L. J., Horton, B. K., & Vallejo, C. (2019). Detrital zircon U-Pb geochronology of modern Andean rivers in Ecuador: Fingerprinting tectonic provinces and assessing downstream propagation of provenance signals. *Geosphere*, *15*(6), 1943–1957. https://doi.org/10.1130/ges02126.1

Jackson, S. E., Pearson, N. J., Griffin, W. L., & Belousova, E. A. (2004). The application of laser ablation-inductively coupled plasma-mass spectrometry to in situ U-Pb zircon geochronology. *Chemical Geology*, *211*(1-2), 47–69. https://doi.org/10.1016/j.chemgeo.2004.06.017

Jarrard, R. D. (1986). Relations among subduction parameters. *Reviews of Geophysics*, *24*(2), 217–284. https://doi.org/10.1029/RG024i002p00217

Johnson, M. N., Jordan, T. E., Johnson, P. A., & Naeser, C. W. (1986). Magnetic polarity stratigraphy, age, and tectonic setting of fluvial sediments in an eastern Andean foreland basin, San Juan Province, Argentina. In P. Allen, & P. Homewood (Eds.), *Foreland basins* (Vol. 8, pp. 63–75). Belgium: IAS Spec. Pub.

Jones, R. E., Kirstein, L. A., Kasemann, S. A., Dhuime, B., Elliott, T., Litvak, V. D., et al. (2015). Geodynamic controls on the contamination of Cenozoic arc magmas in the southern Central Andes: Insights from the O and Hf isotopic composition of zircon. *Geochimica et Cosmochimica Acta*, *164*, 386–402. https://doi.org/10.1016/j.gca.2015.05.007

Jordan, T. E. (1995). Retroarc foreland and related basins. In C. J. Busby, & R. V. Ingersoll (Eds.), *Tectonics of sedimentary basins: Cambridge*, (pp. 331–362). Massachusetts: Blackwell Science.

Jordan, T. E., & Allmendinger, R. W. (1986). The sierras Pampeanas of Argentina: A modern analogue of Rocky Mountain foreland deformation. *American Journal of Science*, *286*, 737–764. https://doi.org/10.2475/ajs.286.10.737

Jordan, T. E., Allmendinger, R. W., Damanti, J. F., & Drake, R. E. (1992). Chronology of motion in a complete thrust belt: The Precordillera 30–31°S. *Andes Mountains, Journal of Geology*, *101*, 135–156. https://doi.org/10.1086/648213

Jordan, T. E., Isacks, B. L., Allmendinger, R. W., Brewer, J. A., Ramos, V. A., & Ando, C. J. (1983). Andean tectonics related to geometry of subducted Nazca plate. *Geological Society of America Bulletin*, *94*(3), 341–361. https://doi.org/10.1130/0016-7606(1983)94<341:ATRTGO>2.0.CO;2

Jordan, T. E., Schlunegger, F., & Cardozo, N. (2001). Unsteady and spatially variable evolution of the Neogene Andean Bermejo foreland basin, Argentina. *Journal of South American Earth Sciences*, *14*, 775–798. https://doi.org/10.1016/s0895-9811(01)00072-4

Jordan, T. E., Tamm, V., Figueroa, G., Flem-Dog, M., Richards, P. B., Tabbutt, K., & Cheatham, T. (1996). Development of the Miocene Manantiales foreland basin, Principal Cordillera, San Juan, Argentina. *Andean Geology*, *23*, 43–79.

Kapp, P., & Decelles, P. G. (2019). Mesozoic–Cenozoic geological evolution of the Himalayan-Tibetan orogen and working tectonic hypotheses. *American Journal of Science*, *319*(3), 159–254. https://doi.org/10.2475/03.2019.01

Kay, S. M., & Abbruzzi, J. M. (1996). Magmatic evidence for Neogene lithospheric evolution of the central Andean "flat-slab" between 30°S and 32°S. *Tectonophysics*, *259*(1-3), 15–28. https://doi.org/10.1016/0040-1951(96)00032-7

Kay, S. M., Godoy, E., & Kurtz, A. (2005). Episodic arc migration, crustal thickening, subduction erosion, and magmatism in the south-Central Andes. *Geological Society of America Bulletin*, *117*(1), 67–88. https://doi.org/10.1130/B25431.1

Kay, S. M., & Mpodozis, C. (2001). Magmatism as a probe to the Neogene shallowing of the Nazca plate beneath the modern Chilean flat-slab. *Journal of South American Earth Sciences*, *15*, 39–57. https://doi.org/10.1016/s0895-9811(02)00005-6

Kay, S. M., Mpodozis, C., Ramos, V. A., & Munizaga, F. (1991). Magma source variations for mid-late tertiary magmatic rocks associated with a shallowing subduction zone and a thickening crust in the Central Andes (28 to 33 S). *Geological Society of America, Special Paper*, *265*, 113–137. https://doi.org/10.1130/SPE265-p113

Kay, S. M., Ramos, V. A., Mpodozis, C., & Sruoga, P. (1989). Late Paleozoic to Jurassic silicic magmatism at the Gondwana margin: Analogy to the middle Proterozoic in North America? *Geology*, *17*(4), 324–328. https://doi.org/10.1130/0091-7613(1989)017<0324:LPTJSM>2.3.CO;2

Kleiman, L. E., & Japas, M. S. (2009). The Choiyoi volcanic province at 34°S-36°S (San Rafael, Mendoza, Argentina): Implications for the Late Paleozoic evolution of the southwestern margin of Gondwana. *Tectonophysics*, *473*(3–4), 283–299. https://doi.org/10.1016/j.tecto.2009.02.046

Lawton, T. F. (2008). *Laramide sedimentary basins, sedimentary basins of the world* (Vol. 5, pp. 429–450). The Netherlands: Elsevier. https://doi.org/10.1016/S1874-5997(08)00012-9

Lawton, T. F., Schellenbach, W. L., & Nugent, A. E. (2014). Late cretaceous fluvial-Megafan and Axial-River systems in the southern cordilleran Foreland Basin: Drip tank member of straight cliffs formation and adjacent strata, southern Utah, U.S.A. *Journal of Sedimentary Research*, *84*, 407–434. https://doi.org/10.2110/jsr.2014.33

Lemos-Santos, D. V., Teixeria, W., Collo, G., & Canelo, H. N. (2019). U-Pb and Sm-Nd constraints on miocene units in the Ischigualasto-Villa Unión foreland basin, sierras Pampeanas, Argentina: Sedimentary provenance, landscape evolution coupling flat-slab subduction. *Journal of South American Earth Sciences*, *90*, 76–93. https://doi.org/10.1016/j.jsames.2018.11.021

Levina, M., Horton, B. K., Fuentes, F., & Stockli, D. F. (2014). Cenozoic sedimentation and exhumation of the foreland basin system preserved in the Precordillera thrust belt (31-32°S), southern Central Andes, Argentina. *Tectonics*, *33*, 1659–1680. https://doi.org/10.1002/2013tc003424

Limarino, C., Tripaldi, A., Marenssi, S., Net, L., Re, G., & Caselli, A. (2001). Tectonic control on the evolution of the fluvial systems of the Vinchina formation (Miocene), northwestern Argentina. *Journal of South American Earth Sciences*, *14*(7), 751–762. https://doi.org/10.1016/S0895-9811(01)00067-0

Link, P. K., Fanning, C. M., & Beranek, L. P. (2005). Reliability and longitudinal change of detrital-zircon age spectra in the Snake River system, Idaho and Wyoming: An example of reproducing the bumpy barcode. *Sedimentary Geology*, *182*(1-4), 101–142. https://doi.org/10.1016/j.sedgeo.2005.07.012

Litvak, V. D., Poma, S., Jones, R. E., Fernández Paz, L., Iannelli, S. B., Spagnuolo, M., et al. (2018). The late Paleogene to Neogene volcanic arc in the southern Central Andes (28°–37°S). In A. Folguera et al. (Eds.), *The evolution of the Chilean-Argentinean Andes* (pp. 503–536). Switzerland: Springer Earth System Sciences. https://doi.org/10.1007/978-3-319-67774-3_20

Löbens, S., Bense, F. A., Dunkl, I., Wemmer, K., Kley, J., & Siegesmund, S. (2013). Thermochronological constraints of the exhumation and uplift of the sierra de pie de Palo, NW Argentina. *Journal of South American Earth Sciences*, *48*, 209–219. https://doi.org/10.1016/j.jsames.2013.09.005

Lossada, A. C., Giambiagí, L., Hoke, G. D., Fitzgerald, P. G., Creixell, C., Murillo, I., et al. (2017). Thermochronologic evidence for late Eocene Andean mountain building at 30°S. *Tectonics*, *36*, 2693–2713. https://doi.org/10.1002/2017TC004674

Mackaman-Lofland, C., Horton, B. K., Fuentes, F., Constenius, K. N., Ketcham, R. A., Capaldi, T. N., et al. (2020). Andean mountain building and foreland basin evolution during thin- and thick-skinned Neogene deformation (32–33°S). *Tectonics*, *39*, e2019TC005838. https://doi.org/10.1029/2019TC005838

Mackaman-Lofland, C., Horton, B. K., Fuentes, F., Constenius, K. N., & Stockli, D. F. (2019). Mesozoic to Cenozoic retroarc basin evolution during changes in tectonic regime, southern Central Andes (31–33°S): Insights from zircon U-Pb geochronology. *Journal of South American Earth Sciences*, *89*, 299–318. https://doi.org/10.1016/j.jsames.2018.10.004

Malkowski, M. A., Sharman, G. R., Johnstone, S., Grove, M. J., Kimbrough, D. L., & Graham, S. A. (2020). Dilution and propagation of provenance trends in sand and mud: Geochemistry and detrital zircon geochronology of modern sediment from Central California (USA). *American Journal of Science*, *319*, 846–902. https://doi.org/10.2475/10.2019.02

Manville, V., Németh, K., & Kano, K. (2009). Source to sink: A review of three decades of progress in the understanding of volcaniclastic processes, deposits, and hazards. *Sedimentary Geology*, *220*(3-4), 136–161. https://doi.org/10.1016/j.sedgeo.2009.04.022

Marenssi, S. A., Limarino, C. O., Schencman, L. J., & Ciccioli, P. L. (2020). Tectonic and geomorphic controls on the lacustrine deposits of the Neogene Vinchina basin, northwestern Argentina. *Journal of Sedimentary Research*, *90*(2), 250–267. https://doi.org/10.2110/jsr.2020.13

Martinod, J., Husson, L., Roperch, P., Guillaume, B., & Espurt, N. (2010). Horizontal subduction zones, convergence velocity and the building of the Andes. *Earth and Planetary Science Letters*, *299*(3-4), 299–309. https://doi.org/10.1016/j.epsl.2010.09.010

Miall, A. D. (1977). A review of the braided-river depositional environment. *Earth-Science Reviews*, *13*(1), 1–62. https://doi.org/10.1016/0012-8252(77)90055-1

Miall, A. D. (1985). Architectural-element analysis: A new method of facies analysis applied to fluvial deposits. *Earth-Science Reviews*, *22*(4), 261–308. https://doi.org/10.1016/0012-8252(85)90001-7

Miall, A. D. (1992). Alluvial deposits. In R. G. Walker, & N. P. James (Eds.), *Facies response to sea-level change* (pp. 119–142). Toronto, Canada: Geological Association of Canada.

Milana, J. P. (1991). *Sedimentología y magnetoestratigrafía de Formaciones Cenozoicas en el área de Mogna, y su inserción en el marco tectosedimentario de la Precordillera Oriental (Doctoral thesis)* (pp. 1–273). San Juan, Argentina: Universidad Nacional de San Juan, Argentina.

Milana, J. P., Bercowski, F., & Jordan, T. E. (2003). Paleoambientes y magnetoestrigrafía del Neógeno de la Sierra de Mogna, y su relación con la Cuenca de Antepaís Andina. *Revista de la Associacion Geologica Argentina*, *38*, 447–473.

Mpodozis, C., & Kay, S. M. (1992). Late Paleozoic to Triassic evolution of the Gondwana margin: Evidence from Chilean frontal cordilleran batholiths (28 S to 31 S). *Geological Society of America Bulletin*, *104*(8), 999–1014. https://doi.org/10.1130/0016-7606(1992)104<0999:LPTTEO>2.3.CO;2

Mulcahy, S. R., Roeske, S. M., McClelland, W. C., Ellis, J. R., Jourdan, F., Renne, P. R., et al. (2014). Multiple migmatite events and cooling from granulite facies metamorphism within the Famatina arc margin of Northwest Argentina. *Tectonics*, *33*, 1–25. https://doi.org/10.1002/2013TC003398

Nemec, W., & Steel, R. J. (1984). Alluvial and coastal conglomerates: Their significant features and some comments on gravelly mass-flow deposits. In *Sedimentology of gravels and conglomerates* (Vol. 10, pp. 1–31). Alberta, Canada: Canadian Society of Petroleum Geologists Memoir.

Odlum, M. L., Stockli, D. F., Capaldi, T. N., Thomson, K. D., Clark, J., Puigdefàbregas, C., & Fildani, A. (2019). Tectonic and sediment provenance evolution of the south eastern Pyrenean foreland basins during rift margin inversion and orogenic uplift. *Tectonophysics*, *765*, 226–248. https://doi.org/10.1016/j.tecto.2019.05.008

Ortiz, G., Alvarado, P., Fosdick, J. C., Perucca, L., Saez, M., & Venerdini, A. (2015). Active deformation in the northern sierra de Valle Fértil, sierras Pampeanas, Argentina. *Journal of South American Earth Sciences*, *64*, 339–350. https://doi.org/10.1016/j.jsames.2015.08.015

Otamendi, J. E., Ducea, M. N., Cristofolini, E. A., Tibaldi, A. M., Camilletti, G. C., & Bergantz, G. W. (2017). U-Pb ages and Hf isotope compositions of zircons in plutonic rocks from the central Famatinian arc, Argentina. *Journal of South American Earth Sciences*, *76*, 412–426. https://doi.org/10.1016/j.jsames.2017.04.005

Painter, C. S., & Carrapa, B. (2013). Flexural versus dynamic processes of subsidence in the north American cordillera foreland basin. *Geophysical Research Letters*, *40*, 4249–4253. https://doi.org/10.1002/grl.50831

Parada, M. A., Nyström, J. O., & Levi, B. (1999). Multiple sources for the coastal batholith of Central Chile (31–34 S): Geochemical and Sr–Nd isotopic evidence and tectonic implications. *Lithos*, *46*(3), 505–521. https://doi.org/10.1016/S0024-4937(98)00080-2

Pepper, M. B., Gehrels, G., Pullen, A., Ibanez-Mejia, M., Ward, K. M., & Kapp, P. (2016). Magmatic history and crustal genesis of South America: Constraints from U-Pb Ages and Hf isotopes of detrital zircons in modern rivers. *Geosphere*, *12*(5), 1532–1555. https://doi.org/10.1130/GES01315.1

Perez, N. D., & Horton, B. K. (2014). Oligocene-Miocene deformational and depositional history of the Andean hinterland basin in the northern Altiplano plateau, Southern Peru. *Tectonics*, *33*, 1819–1847. https://doi.org/10.1002/2014TC003647

Pietras, J. T., & Carroll, A. R. (2006). High-resolution stratigraphy of an Underfilled Lake Basin: Wilkins peak member, Eocene Green River formation, Wyoming, U.S.A. *Journal of Sedimentary Research*, *76*, 1197–1214. https://doi.org/10.2110/jsr.2006.096

Pilger, R. H. (1981). Plate reconstructions, aseismic ridges and low-angle subduction beneath the Andes. *Geological Society of America Bulletin*, *92*(7), 448–456. https://doi.org/10.1130/0016-7606(1981)92<448:PRARAL>2.0.CO;2

Pilger, R. H. (2018). *Radiometric dates from the Andes—Pentecost 2018*. Berlin, Germany: ResearchGate. Available online at https://www.researchgate.net/profile/Rex_Pilger2

Pinto, L., Alarcón, P., Morton, A., & Naipauer, M. (2018). Geochemistry of heavy minerals and U–Pb detrital zircon geochronology in the Manantiales Basin: Implications for frontal cordillera uplift and foreland basin connectivity in the Andes of Central Argentina. *Palaeogeography, Palaeoclimatology, Palaeoecology*, *492*, 104–125. https://doi.org/10.1016/j.palaeo.2017.12.017

Porter, R., Gilbert, H., Zandt, G., Beck, S., Warren, L., Calkins, J., et al. (2012). Shear wave velocities in the Pampean flat-slab region from Rayleigh wave tomography: Implications for slab and upper mantle hydration. *Journal of Geophysical Research*, *117*, 1–21. https://doi.org/10.1029/2012JB009350

Pysklywec, R. N., & Mitrovica, J. X. (1999). The role of subduction-induced subsidence in the evolution of the Karoo Basin. *Journal of Geology*, *107*(2), 155–164. https://doi.org/10.1086/314338

Ramos, V. A. (1999). Plate tectonic setting of the Andean cordillera. *Episodes*, *22*(3), 183–190. https://doi.org/10.18814/epiiugs/1999/v22i3/005

Ramos, V. A. (2004). Cuyania, an exotic block to Gondwana: Review of a historical success and the present problems. *Gondwana Research*, *7*(4), 1009–1026. https://doi.org/10.1016/S1342-937X(05)71081-9

Ramos, V. A. (2009). Anatomy and global context of the Andes: Main geologic features and the Andean orogenic cycle. In S. M. Kay, V. A. Ramos, & W. R. Dickinson (Eds.), *Backbone of the Americas: Shallow subduction, plateau uplift, and ridge and terrane collision* (Vol. 204, pp. 31–65). CO, USA: Geological Society of America Memoir.

Ramos, V. A., Cristallini, E. O., & Perez, D. J. (2002). The Pampean flat-slab of the Central Andes. *Journal of South American Earth Sciences*, *15*(1), 59–78. https://doi.org/10.1016/S0895-9811(02)00006-8

Ramos, V. A., & Folguera, A. (2009). Andean flat-slab subduction through time. *Geological Society, London, Special Publications*, *327*(1), 31–54. https://doi.org/10.1144/SP327.3

Ramos, V. A., Litvak, V. D., Folguera, A., & Spagnuolo, M. (2014). An Andean tectonic cycle: From crustal thickening to extension in a thin crust (34°-37°SL). *Geoscience Frontiers*, *5*, 351–367. https://doi.org/10.1016/j.gsf.2013.12.009

Ranero, C. R., von Huene, R., Weinrebe, W., & Reichert, C. (2006). Tectonic processes along the Chile convergent margin. *In The Andes*, (pp. 91–121). Berlin, Heidelberg: Springer. https://doi.org/10.1007/978-3-540-48684-8_5

Rapela, C. W., Pankhurst, R. J., Casquet, C., Fanning, C. M., Baldo, E. G., González-Casado, J. M., et al. (2007). The Río de la Plata craton and the assembly of SW Gondwana. *Earth-Science Reviews*, *83*(1–2), 49–82. https://doi.org/10.1016/j.earscirev.2007.03.004

Rapela, C. W., Verdecchia, S. O., Casquet, C., Pankhurst, R. J., Baldo, E. G., Galindo, C., et al. (2016). Identifying Laurentian and SW Gondwana sources in the Neoproterozoic to early Paleozoic metasedimentary rocks of the sierras Pampeanas: Paleogeographic and tectonic implications. *Gondwana Research*, *32*, 193–212. https://doi.org/10.1016/j.gr.2015.02.010

Reynolds, J. H., Jordan, T. E., Johnson, N. M., Damanti, J. F., & Tabbutt, K. D. (1990). Neogene deformation of the flat-subduction segments of the argentine-Chilean Andes: Magnetostratigraphic constraints from Las juntas, La Rioja province, Argentina. *Geological Society of America Bulletin*, *102*(12), 1607–1622. https://doi.org/10.1130/0016-7606(1990)102<1607:NDOTFS>2.3.CO;2

Riesner, M., Simoes, M., Carrizo, D., & Lacassin, R. (2019). Early exhumation of the frontal cordillera (southern Central Andes) and implications for Andean mountain-building at ~33.5°S. *Scientific Reports*, *9*(7972). https://doi.org/10.1038/s41598-019-44320-1

Rubey, M., Brune, S., Heine, C., Rhodri Davies, D., Williams, S. E., & DIetmar Müller, R. (2017). Global patterns in Earth's dynamic topography since the Jurassic: The role of subducted slabs. *Solid Earth*, *8*(5), 899–919. https://doi.org/10.5194/se-8-899-2017

Ruskin, B. G., & Jordan, T. E. (2007). Climate change across continental sequence boundaries: Paleopedology and Lithofacies of Iglesia Basin, Northwestern Argentina. *Journal of Sedimentary Research*, *77*(9), 661–679. https://doi.org/10.2110/jsr.2007.069

Saleeby, J. (2003). Segmentation of the Laramide slab—Evidence from the southern Sierra Nevada region. *Geological Society of America Bulletin*, *115*(6), 655–668. https://doi.org/10.1130/0016-7606(2003)115<0655:SOTLSF>2.0.CO;2

Schellart, W. P. (2017). Andean mountain building and magmatic arc migration driven by subduction-induced whole mantle flow. *Nature Communications*, *8*(1), 2010–2013. https://doi.org/10.1038/s41467-017-01847-z

Schellart, W. P., Freeman, J., Stegman, D. R., Moresi, L., & May, D. (2007). Evolution and diversity of subduction zones controlled by slab width. *Nature*, *446*, 308–7133. https://doi.org/10.1038/nature05615

Schwartz, J. J., Gromet, L. P., & Miro, R. (2008). Timing and duration of the calc-alkaline arc of the Pampean orogeny: Implications for the late Neoproterozoic to Cambrian evolution of Western Gondwana. *The Journal of Geology*, *116*(1), 39–61. https://doi.org/10.1086/524122

SEGEMAR (1999). *Geologia Argentina, scale 1:3,000,000, version digital en CD-ROM*. Buenos Aires, Argentina: SEGEMAR.

SEGEMAR (2012). *Sistema de información geográfica del servicio geológico minero Argentino*. Buenos Aires, Argentina: SEGEMAR.

Sernageomin (2003). *Mapa geologico de Chile: Version digital. Mapa escala 1:1,000,000* (Vol. 4, p. 25). Santiago, Chile: Sernageomin.

Sláma, J., Košler, J., Condon, D. J., Crowley, J. L., Gerdes, A., Hanchar, J. M., et al. (2008). Plešovice zircon—A new natural reference material for U–Pb and Hf isotopic microanalysis. *Chemical Geology*, *249*(1–2), 1–35. https://doi.org/10.1016/j.chemgeo.2007.11.005

Smith, G. A., & Lowe, D. R. (1991). Lahars: Volcano-hydrologic events and deposition in the debris flow-hyperconcentrated flow continuum. In *Sedimentation in volcanic settings* (pp. 59–70). OK, USA: SEPM.

Stevens-Goddard, A. L., & Carrapa, B. (2017). Using basin thermal history to evaluate the role of Miocene–Pliocene flat-slab subduction in the southern Central Andes (27°S–30°S). *Basin Research*, *30*(3), 564–585. https://doi.org/10.1111/bre.12265

Stevens-Goddard, A. L., Larrovere, M. A., Carrapa, B., Aciar, R. H., & Alvarado, P. (2018). Reconstructing the thermal and exhumation history of the sierras Pampeanas through low-temperature thermochronology: A case study from the sierra de Velasco. *GSA Bulletin*, *130*(11–12), 1842–1858. https://doi.org/10.1130/B31935.1

Suriano, J., Mardonez, D., Mahoney, J. B., Mescua, J. F., Giambiagí, L. B., Kimbrough, D., & Lossada, A. (2017). Uplift sequence of the Andes at 30°S: Insights from sedimentology and U/Pb dating of synorogenic deposits. *Journal of South American Earth Sciences*, *75*, 11–34. https://doi.org/10.1016/j.jsames.2017.01.004

Thomas, W. A., Astini, R. A., Mueller, P. A., & McClelland, W. (2015). Detrital-zircon geochronology and provenance of the Ocloyic synorogenic clastic wedge, and Ordovician accretion of the argentine Precordillera terrane. *Geosphere*, *11*(6), 1749–1769. https://doi.org/10.1130/GES01212.1

Tripaldi, A., & Limarino, C. O. (2005). Vallecito formation (Miocene): The evolution of an eolian system in an Andean foreland basin (northwestern Argentina). *Journal of South American Earth Sciences*, *19*(3), 343–357. https://doi.org/10.1016/j.jsames.2005.04.006

Val, P., Hoke, G. D., Fosdick, J. C., & Wittmann, H. (2016). Reconciling tectonic shortening, sedimentation and spatial patterns of erosion from 10Be paleo-erosion rates in the argentine Precordillera. *Earth and Planetary Science Letters*, *450*, 173–185. https://doi.org/10.1016/j.epsl.2016.06.015

van Hunen, J., Van Den, B. E. R. G., & A. P. and Vlaar, N. J. (2002). On the role of subducting oceanic plateaus in the development of shallow flat subduction. *Tectonophysics*, *352*(3–4), 317–333. https://doi.org/10.1016/S0040-1951(02)00263-9

Vergés, J., Ramos, E., Seward, D., Busquets, P., & Colombo, F. (2001). Miocene sedimentary and tectonic evolution of the Andean Precordillera at 31°S, Argentina. *Journal of South American Earth Sciences*, *14*(7), 735–750. https://doi.org/10.1016/S0895-9811(01)00070-0

von Gosen, W. (1992). Structural evolution of the argentine Precordillera: The Rio San Juan section. *Journal of Structural Geology*, *14*, 643–667. https://doi.org/10.1016/0191-8141(92)90124-f

Wagner, L. S., Beck, S., & Zandt, G. (2005). Upper mantle structure in the south central Chilean subduction zone (30° to 36°S). *Journal of Geophysical Research, Solid Earth*, *110*(B1), 1, B01308–20. https://doi.org/10.1029/2004JB003238

Wagner, L. S., Beck, S., Zandt, G., & Ducea, M. N. (2006). Depleted lithosphere, cold, trapped asthenosphere, and frozen melt puddles above the flat slab in Central Chile and Argentina. *Earth and Planetary Science Letters*, *245*(1-2), 289–301. https://doi.org/10.1016/j.epsl.2006.02.014

Walcek, A. A., & Hoke, G. D. (2012). Surface uplift and erosion of the southernmost argentine Precordillera. *Geomorphology*, *153-154*, 156–168. https://doi.org/10.1016/j.geomorph.2012.02.021

Ward, K. M., Porter, R. C., Zandt, G., Beck, S. L., Wagner, L. S., Minaya, E., & Tavera, H. (2013). Ambient noise tomography across the Central Andes. *Geophysical Journal International*, *194*(3), 1559–1573. https://doi.org/10.1093/gji/ggt166

Wiedenbeck, M. A. P. C., Alle, P., Corfu, F., Griffin, W. L., Meier, M., Oberli, F. V., et al. (1995). Three natural zircon standards for U-Th-Pb, Lu-Hf, trace element and REE analyses. *Geostandards Newsletter*, *19*(1), 1–23. https://doi.org/10.1111/j.1751-908X.1995.tb00147.x

Yáñez, G. A., Ranero, C. R., Huene, R., & Díaz, J. (2001). Magnetic anomaly interpretation across the southern Central Andes (32–34 S): The role of the Juan Fernández ridge in the late tertiary evolution of the margin. *Journal of Geophysical Research*, *106*(B4), 6325–6345. https://doi.org/10.1029/2000JB900337

Yin, A., & Ingersoll, R. V. (1997). A model for evolution of Laramide axial basins in the southern Rocky Mountains, USA. *International Geology Review*, *39*(12), 1113–1123. https://doi.org/10.1080/00206819709465318

Zapata, T. R., & Allmendinger, R. W. (1996). Thrust-front zone of the Precordillera, Argentina: A thick-skinned triangle zone. *AAPG Bulletin*, *80*, 359–381. https://doi.org/10.1306/64ed87e6-1724-11d7-8645000102c1865d